Proceedings of ASME Turbo Expo 2011
GT2011
June 6-10, 2011, Vancouver, British Columbia, Canada

GT2011-46124

THE NUMERICAL SIMULATION OF INLET FOGGING EFFECTS ON THE STABLE RANGE OF A TRANSONIC COMPRESSOR STAGE

Mingcong Luo, Qun Zheng, Lanxin Sun, Qingfeng Deng, Song Li and Chunlei Liu
Harbin Engineering University, Harbin 150001, China
Rakesh K. Bhargava[+]
[+]Turbomachinery Consultant, Houston, USA
E-mail: trylove39@163.com.cn, zhengqun@hrbeu.edu.cn

ABSTRACT

The inlet fogging effects on the stable range of a NASA transonic compressor stage, Stage 35, are numerically simulated and analyzed in this paper. The 3-D two-phase flow fields in the compressor stage are investigated under different operating flow conditions with varying levels of the injected water flow rates and the fogging droplets sizes. The special attention is given to the stall and the choking operating points to investigate changes in the stable operating range of the compressor stage as a result of different wet compression conditions. The preliminary results indicate that the inlet fogging has different effects on either the stall and/or the choking range. The change in the stable range of this transonic compressor stage depends on the fogging flowrate and droplets diameters.

Key words: Transonic compressor stage; Inlet fogging; Numerical simulation; Stall boundary; Choking boundary.

INTRODUCTION

The use of water injection technique into the compressor has shown to increase the power output of a gas turbine. It has become a useful power augmentation technology [1-5]. In recent years, a number of studies were carried out to better understand the main features of the inlet fogging technologies. This increasing attention could be explained by considering that inlet fogging is a simple and effective approach [6]. Inlet fogging has been implemented in simple and combined cycle applications and nowadays, it could be considered consolidated technologies [7]. It has been applied in power generation industry [7-10]. There are some experiments about the overall gas turbine performances with wet compression and the design of fogging systems and the corresponding industrial application techniques have been researched as well [11-17]. However, the measurements of flow fields in the compressor blade passages with discrete water droplets are very difficult due to the complicated two-phase flows and phase change process in the rotating turbomachinery [18, 19]. Although more and more attentions have been paid to the related theoretical studies [20-25], the effects of wet compression on the stall boundary and choking boundary needs to be thoroughly investigated for safe working of the compressor and the gas turbine unit.

The available literature shows that the effects of wet compression on performance of a transonic compressor stage, a stage commonly used in a high-pressure ratio compressor with high stage loading, including effects on the stable flow range are not fully examined. Furthermore, analytical studies available in the literature have not investigated effects of the wet compression under 3-D flow conditions. Therefore, in this study, the numerical simulation has been conducted to investigate effects of the wet compression on the performance of a transonic compressor stage with particular emphasis to the stall and choking operational conditions. The numerical simulation study, conducted on an isolated transonic compressor stage (NASA Stage 35), is performed using commercially available Computational Fluid Dynamic (CFD) analysis software (ANSYS CFX). The effects of water injection flowrates and the droplets sizes are investigated on the 3-D flow fields within both the blade passages of the transonic compressor stage with the stage operating at different flow conditions including stall and chocking points.

MODEL COMPRESSOR

A low-aspect-ratio transonic compressor stage, NASA Stage 35, was chosen for the present study. As a well-known test case, this isolated stage was originally designed and tested at the NASA Lewis Research Center in the late 1970's by Reid and Moore [26-28]. The design parameters of the selected compressor stage are summarized in Table 1.

Table 1 Design parameters of NASA Stage 35 [27]	
Number of rotor blades	36
Number of stator blades	46
Stage inlet hub-to-tip radius ratio	0.7
Rotor blade aspect ratio	1.19
Stator blade aspect ratio	1.26
Design tip clearance (mm)	0.2
Design mass flow rate (kg/s)	20.19
Design rotational speed (rpm)	17188.7
Tip speed (m/s)	454.5
Reference pressure (Pa)	101,325
Rotor total pressure ratio	1.865
Stage total pressure ratio	1.820
Stage total temperature ratio	1.225
Stage adiabatic efficiency	0.828
Stage stall margin at design speed (%)	21.8

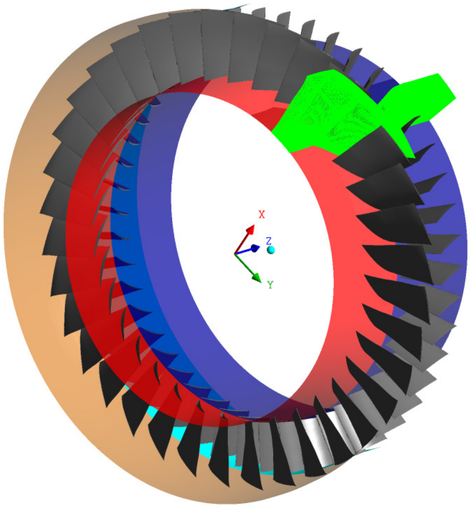

(a) Geometric model

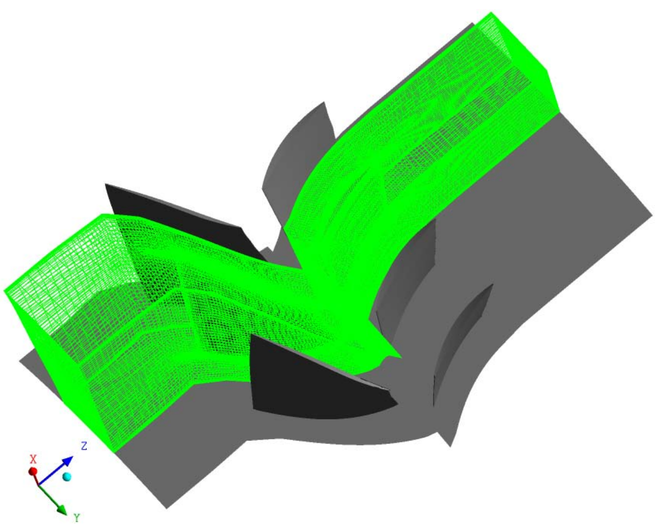

(b) Computational domain

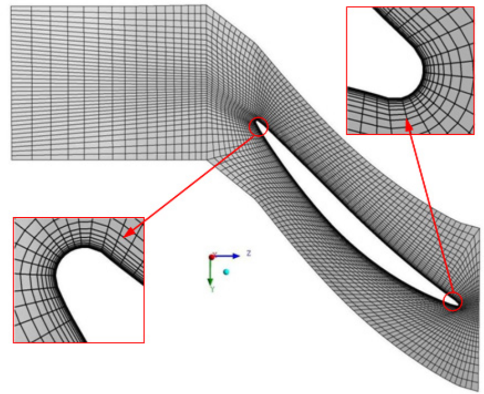

(c) Rotor blade-to-blade mesh view

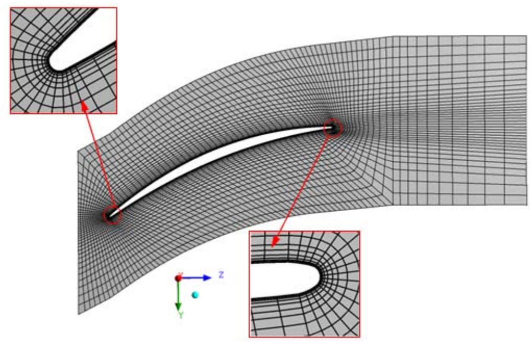

(d) Stator blade-to-blade mesh view

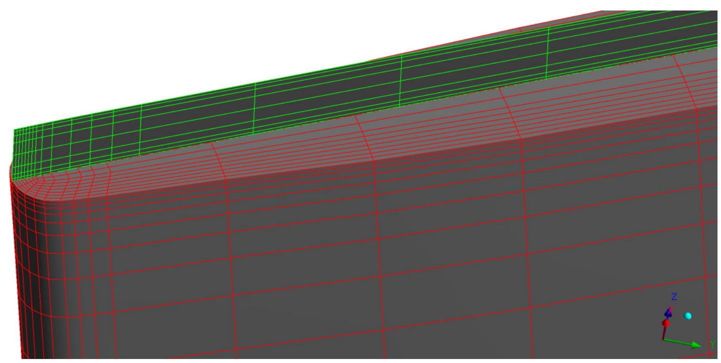

(e) Tip clearance mesh near the rotor blade leading edge

Fig. 1 Computational geometric model and grids for NASA Stage 35

The geometric model for NASA Stage 35 is displayed in Figure 1a. A multi-block structured grid of about 760,000 elements (Figure 1b) was applied to discretize the computational domain. A high-quality H-type grid was adopted for both inlet and outlet blocks, while an advanced J-type grid was utilized for the blade passage block with 10 layers of O-type grid around the blade (Figure 1c and Figure 1d) leading edge to achieve a good flow field representation. The tip-clearance region was also considered with 10 grid elements in spanwise direction (Figure 1e).

TURBULENCE MODEL AND BOUNDARY CONDITIONS

In order to simulate the complicated turbulent flows correctly in this transonic compressor stage, a well-suited turbulence model should be selected carefully. The realizable $k-\varepsilon$ turbulence model is chosen in this paper for its extensive validation for a wide range of flows, including rotational flows, boundary-layer flows under strong adverse pressure gradients, separated flows, etc. [21].

The transport equations of the realizable $k-\varepsilon$ turbulence model are:

$$\frac{\partial}{\partial t}(\rho\varepsilon)+\frac{\partial k}{\partial x_j}(\rho\varepsilon u_j)=\frac{\partial}{\partial x_j}\left[\left(\mu+\frac{\mu_t}{\sigma_\varepsilon}\right)\frac{\partial \varepsilon}{\partial x_j}\right]-\rho C_2\frac{\varepsilon^2}{k+\sqrt{\upsilon\varepsilon}} \tag{1}$$

$$\frac{\partial}{\partial t}(\rho k)+\frac{\partial k}{\partial x_j}(\rho k u_j)=\frac{\partial}{\partial x_j}\left[\left(\mu+\frac{\mu_t}{\sigma_k}\right)\frac{\partial k}{\partial x_j}\right]+G_k-\rho\varepsilon \tag{2}$$

where, G_k represents the generation of turbulence kinetic energy due to the velocity gradients, C_2 and $C_{1\varepsilon}$ are constants, σ_k is the Prandtl number for k and σ_ε is the turbulent Prandtl number for ε.

The eddy viscosity is computed from

$$\mu_t=\rho C_\mu\frac{k^2}{\varepsilon}\text{, and } C_\mu=\frac{1}{A_0+A_s\dfrac{kU^*}{\varepsilon}},$$

The model constants A_0 and A_s are given by

$$A_0=4.04,\ A_s=\sqrt{6}\cos\phi,$$

The values of various model constants are: $C_{1\varepsilon}=1.44$, $C_2=1.92$, $\sigma_k=1.0$, $\sigma_\varepsilon=1.2$ [30].

The values of total temperature and the total pressure assumed at the compressor stage inlet boundary are 298.15K and 101325 Pa, respectively. In this numerical calculation, the air at the inlet boundary is assumed dry. On the hub, shroud and blade surfaces no slip (the fluid immediately next to the wall assumes the velocity of the wall, which is zero by default) and adiabatic (the heat flux across the wall boundary is zero) conditions were imposed. The static pressure was specified at the compressor stage exit boundary. At the design, the stall and the choking points, all the numerical simulations were carried out for both dry and wet cases.

The calculation is started first with the stator outlet static pressure of 10450 Pa. The calculated flowrate is close to the measured maximum flowrate under this condition and this operating point is defined as the chocking flow point. Then the stator outlet static pressure is increased step-by-step. The step size is assumed big at first, and then the step size becomes small until 10 Pa when it is near stall and this method can be used to determine the stall point at which the outlet static pressure is 52450 Pa.

Figure 2 shows a comparison of the stage performance characteristic curve, obtained using the $k-\varepsilon$ turbulence model, with the experimental data [27] at the design rotating speed. The flowrate normalized by the maximum flowrate is shown on the abscissa. It can be seen that compared to the experiment data, the stable operating range of numerical result narrows down especially in large amount at the stall boundary. However, the pressure ratio values are in general lower than the experiment data. It must be noted that the stage pressure ratio value at the design point, obtained through the numerical simulation, is reasonably in good agreement with the experimental data.

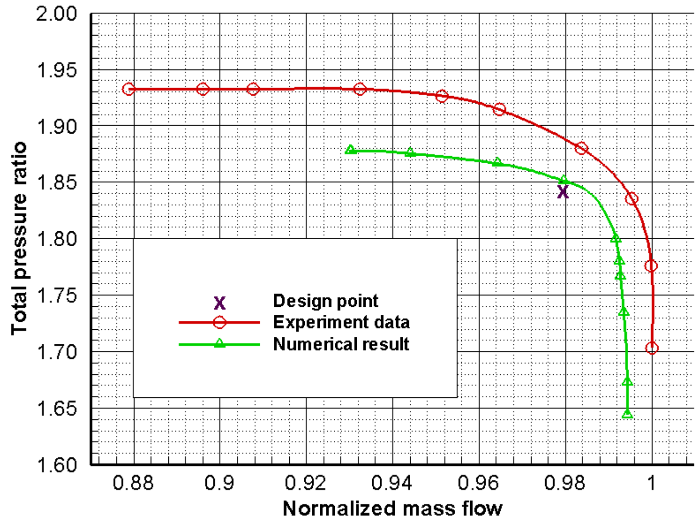

Fig. 2 Contrast of simulated results of the $k-\varepsilon$ turbulence models with experimental data

NUMERICAL SIMULATIONS AND RESULTS

The simulations are carried out for different fogging flowrates and the droplet diameters.

(1) Simulations are implemented for different fogging flowrates ranging from 0.5 percent to 2 percent with the increment by 0.5 percent of the inlet mass flowrate.

(2) The fogging droplet diameter spectrum is 3, 5, 8, 10 and 15 μm.

Figure 3 shows dry and wet stage performance characteristic lines under different values of fogging droplet diameters and flowrates. In Fig. 3(a) and Fig. 3(b), compared to the dry performance characteristic line, inlet fogging for droplets size of 5 micron will generally expand the stall boundary to lower normalized mass flow, but narrow the choking boundary to lower normalized mass flow. With the increasing of the fogging flowrate, the mass flow of the choking boundary will be decreased while the mass flow of the stall boundary will be increased. Figure 3(a) shows that the inlet fogging could improve the total pressure ratio, compared to the dry case, if the mass flow is less than the mass flow at design point and the stage total pressure ratio increases with the increase in the fogging flowrate. For a given droplet size, Fig. 3(b) also shows that inlet fogging could improve the stage adiabatic efficiency compared to the dry case with increase in the fogging flowrate.

As shown in Fig. 3(c) and Fig. 3(d), if we keep the inlet fogging flowrate constant at 2% and increase the droplets size from 5 micron to 8, 10 and 15 microns respectively, it is found that the choking boundary moves to a nearly same normalized mass flow, and the stall boundary moves to a higher mass flow except for the 5 micron case. The total pressure ratio of 15 micron characteristic line decreases compared with dry characteristic line in the whole working range. For a given amount of inlet fogging flow rate, the stage adiabatic efficiency is improved by decreasing the droplet size as shown in Fig. 3(d).

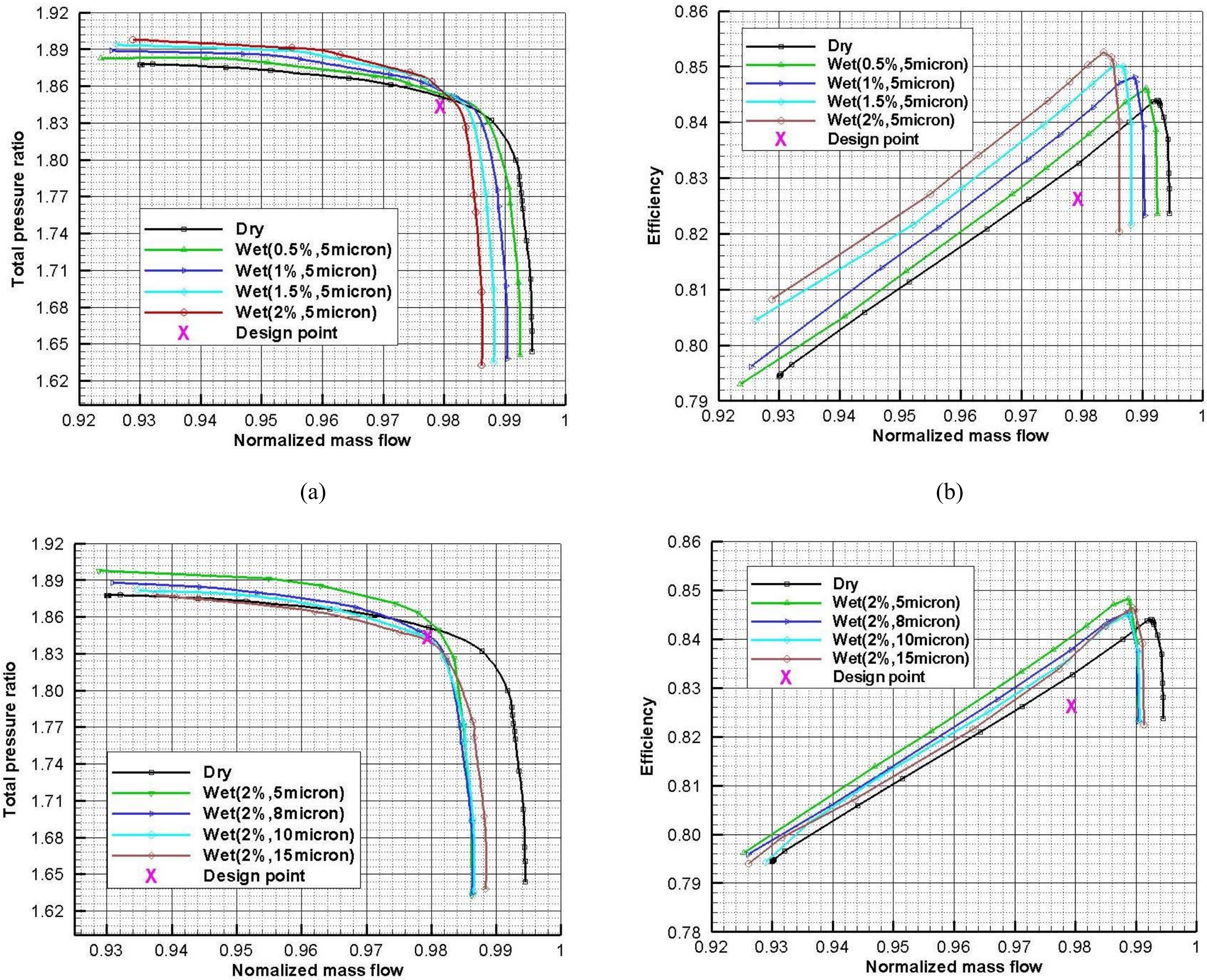

(a) (b)

(c) (d)

Fig. 3 Comparison of simulated results for the wet and dry stage performance characteristic curves

1. Stage performance with inlet fogging at the stall boundary of dry compression

Figure 4 shows effects on the inlet total mass flowrate under different fogging mass flowrates and droplets diameters with each case at the stall operating point under dry condition. The dry mass flow rate at the stall point has a value of 19.33 kg/s as shown in Fig. 4. For a given droplet size, inlet mass flow rate increases with the increase in the amount of fogging flow rate (see Fig. 4). In the cases with droplets sizes of 10 and 15 micron, the inlet mass flowrates are greater than that for the dry compression. However, in the cases of 3 micron and 5 micron, the inlet mass flowrate is smaller than that of dry compression. The mass flowrate is basically unchanged under the condition of 8 micron inlet fogging. The results also indicate that the droplet size has an effect on the movements of the stall boundary and the moving direction depends on the size of the fogging droplet.

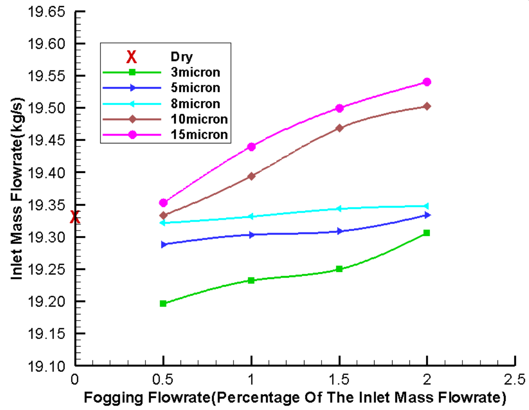

Fig. 4 Comparison of inlet mass flowrates at dry and wet cases boundary

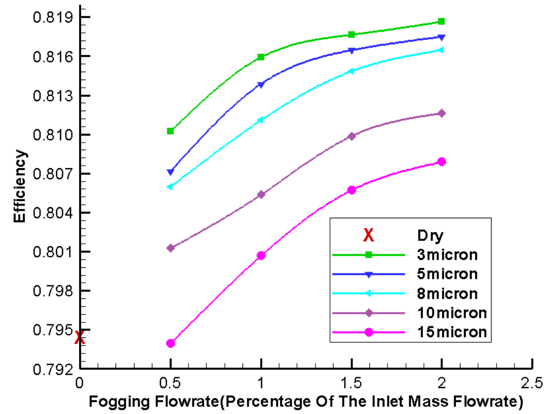

Fig. 5 Comparison of the stage adiabatic efficiency under dry and wet conditions – All dry cases at the stall boundary

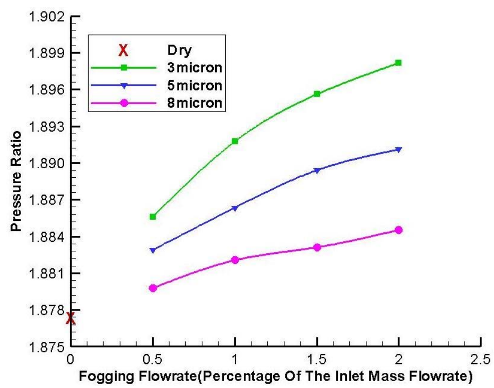

(a)

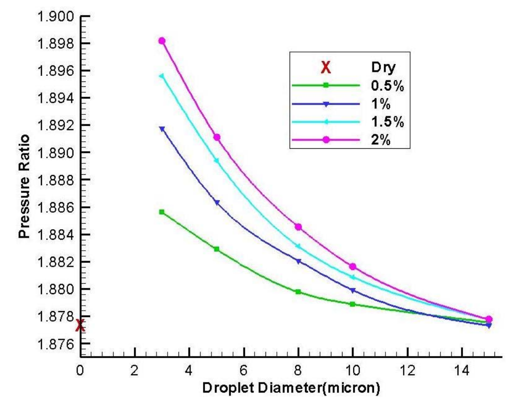

(b)

Fig. 6 Comparison of the stage total pressure ratio under dry and wet conditions – All dry cases at the stall boundary

To calculate the stage adiabatic efficiency under wet compression, it is necessary to calculate the ideal wet compression work. The dry air and water vapor are considered as ideal-gases and are compressed from p_{t1} to p_{t2} respectively.

The wet compression efficiency is given by

$$\eta_w = \frac{W_{wi}}{W_w} \quad (3)$$

where, W_{wi} and W_w is isentropic and actual specific work of wet compression respectively, W_{wi} and W_w are written as:

$$W_{wi} = (W_a + fW_v)/(1+f) \quad (4)$$

$$W_w = \omega M_t / m_{in} \quad (5)$$

where, ω is the rotating speed, f is steam to air (or water to air) ratio, m_{in} is stage inlet mass flowrate, M_t is the torque on the rotor, W_a and W_v is specific compression work of gas and vapor component respectively, W_a and W_v are defined as:

$$W_a = (h_{t2,i} - h_{t1})_a = C_{pa} T_{t1} \left[\left(\frac{p_{t2}}{p_{t1}} \right)^{\frac{\gamma_a - 1}{\gamma_a}} - 1 \right], \quad (6)$$

$$W_v = (h_{t2,i} - h_{t1})_v = C_{pv} T_{t1} \left[\left(\frac{p_{t2}}{p_{t1}} \right)^{\frac{\gamma_v - 1}{\gamma_v}} - 1 \right] \quad (7)$$

where, subscript a and v represent air and vapor component respectively, subscript 1 and 2 represent stage inlet and outlet respectively. C_p is the constant pressure specific heat, T_{t1} is temperature at stage inlet and γ is the ratio of specific heats.

Figure 5 shows the comparison of efficiency for dry and wet cases under different fogging flowrates and droplet sizes at stall boundary of the dry case. It can be seen that the efficiency of wet cases are mostly higher than the dry case (0.7944) except for one operating point case (0.7939) in which the fogging flowrate is 0.5% and droplet diameter is 15 micron. It means that fogging droplet size of injecting to this single-stage axial-flow transonic compressor could not be too big. In this picture, it is also noticed that efficiency could be improved with the increased fogging flowrate (for the droplet diameter of 5 micron, the efficiency values at 0.5% and 2% of the inlet mass flow are 0.8071 and 0.8175, respectively.) and the decreased droplet size (for fogging flowrate of 1% of the inlet air mass flow, the stage adiabatic efficiency values with droplet diameters of 10 microns and 5 microns are 0.8053 and 0.8139, respectively). The efficiency curves become flat when the fogging flowrate is 2% of inlet mass flow (the efficiency of 3 micron is 0.8187 and the 5 micron is 0.8175).

Figure 6 shows the pressure ratios of the transonic compressor stage under different fogging flowrates and different droplet diameters where in each case dry case is at the stall operating point. Compared to the dry compression, the inlet fogging could improve the pressure ratio. It also can be seen that the pressure ratio could be improved by increasing the fogging flowrate or decreasing the droplet diameter. If the droplet diameter is bigger than a certain size, the inlet fogging has a little effect on the pressure ratio compared to the dry case as shown in Fig. 6(b).

Figure 7 shows the change in stage outlet total temperature. The stage outlet temperature reduces with the decrease in the fog droplets size at a constant value of the fogging flow rate. For a given droplet diameter, the stage outlet temperature decreases, compared to the dry case, with increase in the fogging flow rate as shown in Fig. 7(a). In Fig.7(a) the outlet total temperature decreases from 353.4K (0.5%, 3micron) to 341.7K (2%, 3micron) in the investigated range of fogging flow. As shown in Fig. 7(b), the temperature decreases from 357.5K (2%, 15micron) to 341.8K (2%, 3micron).

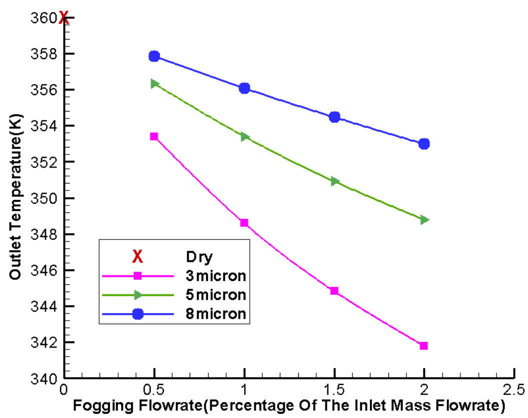

(a)

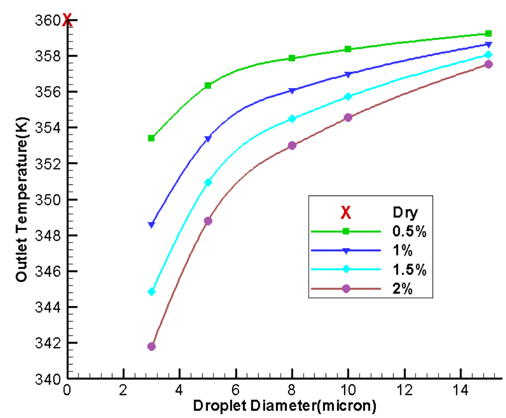

(b)

Fig. 7 Comparison of outlet temperature under dry and wet conditions – All dry cases at the stall boundary

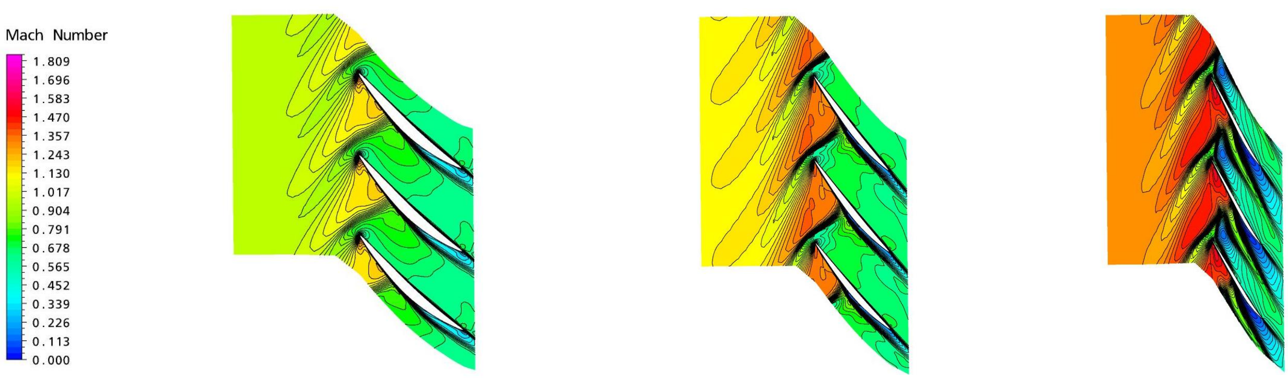

(a) Dry case (Span: left 5%; mid 50%; right 97%)

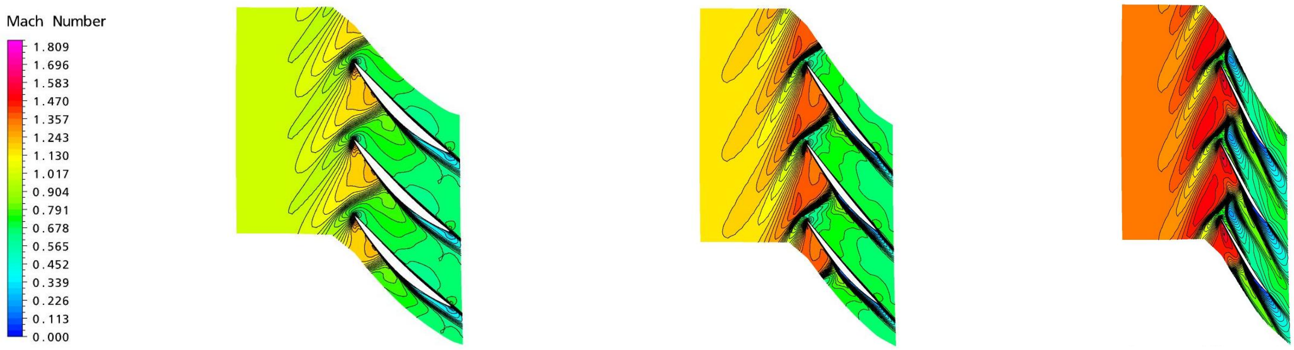

(b) Wet case (Span: left 5%; mid 50%; right 97%)
(Inlet injection: R-R size 10μm; 0.5% of the inlet total mass flowrate)

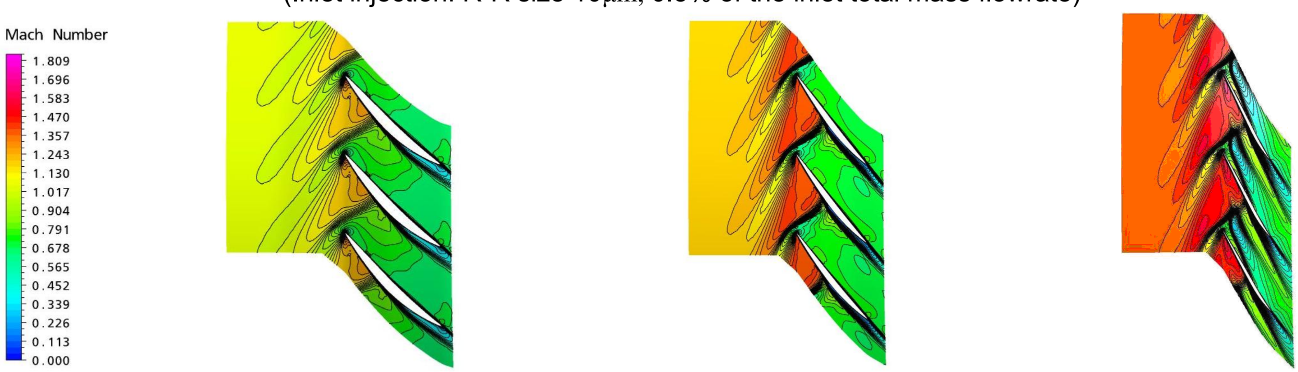

(c) Wet case (Span: left 5%; mid 50%; right 97%)
(Inlet injection: R-R size 10μm; 1% of the inlet total mass flowrate)

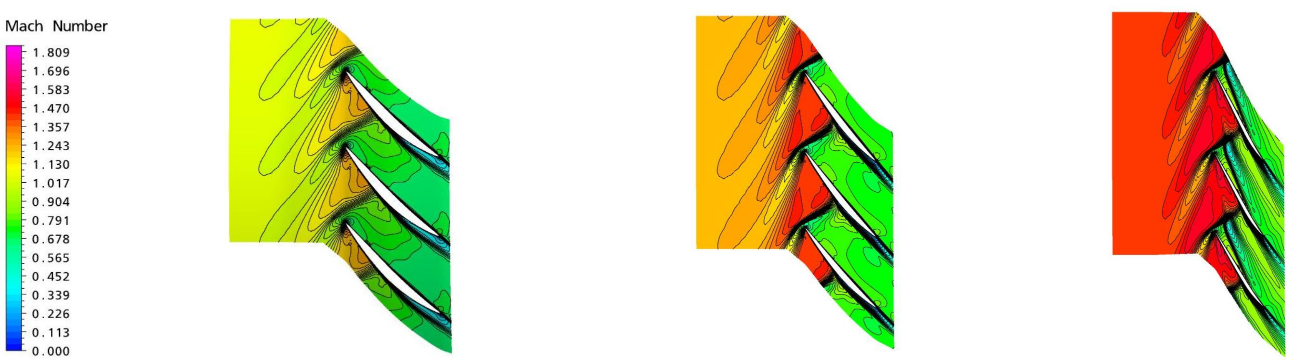

(d) Wet case (Span: left 5%; mid 50%; right 97%)
(Inlet injection: R-R size 10μm; 2% of the inlet total mass flowrate)
Fig. 8 Contours of Mach number on rotor blade to blade surfaces under the same injected droplet size – All dry cases at the stall boundary

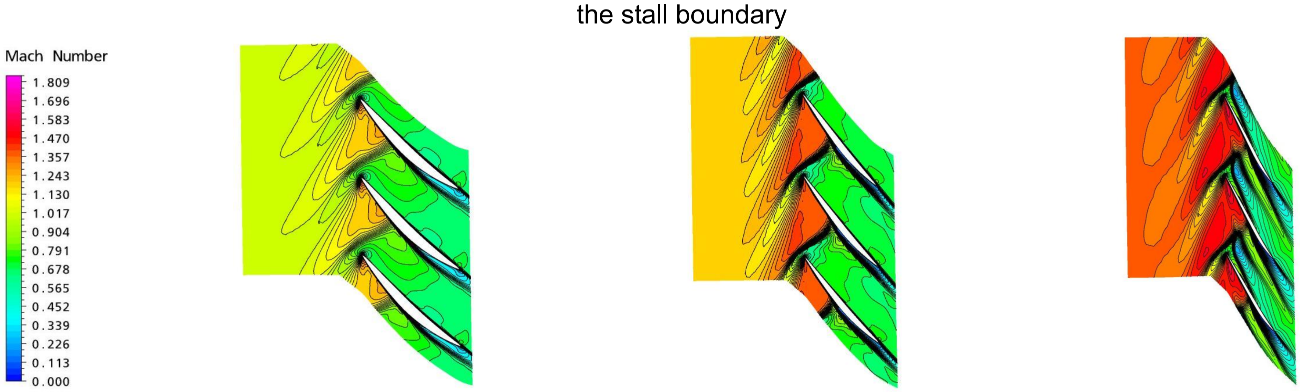

(a) Wet case (Span: left 5%; mid 50%; right 97%)
(Inlet injection: R-R size 8μm; 0.5% of the inlet total mass flowrate)

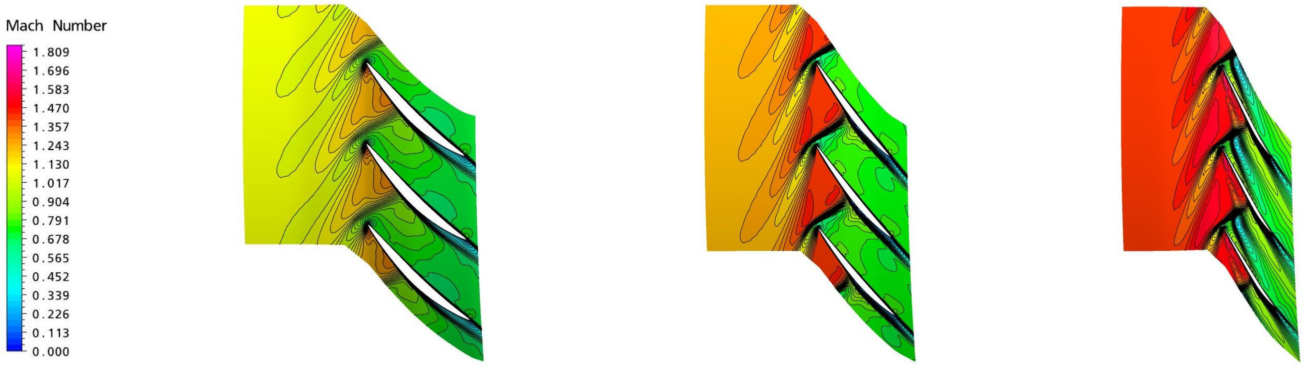

(b) Wet case (Span: left 5%; mid 50%; right 97%)
(Inlet injection: R-R size 5μm; 0.5% of the inlet total mass flowrate)

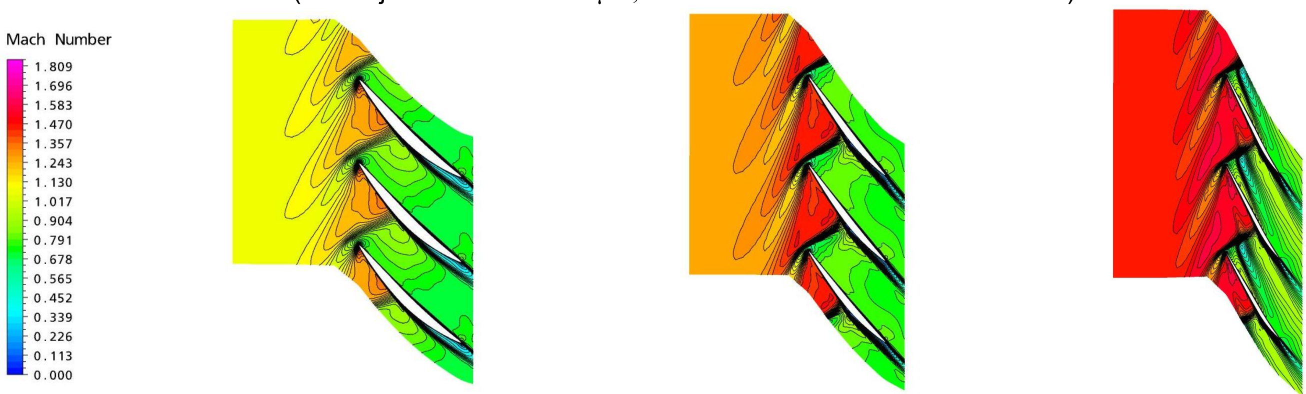

(c) Wet case (Span: left 5%; mid 50%; right 97%)
(Inlet injection: R-R size 3μm; 0.5% of the inlet total mass flowrate)

Fig. 9 Contours of Mach number on rotor blade to blade surfaces under the same fogging flowrate – All dry cases at the stall boundary

Figures 8 presents the contours of Mach number on the rotor blade-to-blade surfaces under same injected droplet size (10 μm) but with different amount of fogging flowrate including the dry case at the three spanswise locations Whereas, the contours of Mach number on the rotor blade surface with the same fogging flowrate (0.5%) but different droplet size at the three spanwise locations are shown in Fig. 9. Figure 10 shows the contours of Temperature on the rotor blade-to-blade surfaces for dry and wet cases under same droplet size but with different fogging flowrates.

In Fig. 8 and Fig. 9, it can be seen that the difference of contours for Mach number especially on the surfaces of span 5% and 50% are not evident among wet cases and dry case. This happened due to the small evaporation rate under a low temperature field. On the blade-to-blade surface of span 97%, inlet fogging could change shape of the shock wave and make the shock wave moving to the middle of flow passage. Compared to the dry case, inlet fogging also improves the Mach number behind the shock wave and reduces the stall region evidently. It certainly proves that the inlet fogging improved the flow field and inhibited the stall of this transonic compressor stage. Fig. 8 and Fig. 9 also show that Mach number is increased behind the shock wave and the stall region is reduced with the gradually increasing of fogging flowrate or decreasing of droplets diameter.

From Fig. 10, it can be seen that the temperature downstream of the shock wave on the rotor blade-to-blade surfaces of span 5%, 50% and 97% of wet cases are lower than the dry case. It also can be seen that the differences in temperature contours especially on the surfaces of span 50% and 97% are evident among dry and wet cases. As shown in Fig. 10, the increase in fogging flowrate or decrease in droplet diameters significantly reduces the temperature downstream of the shock wave.

To analyze the relative total pressure loss, it is necessary to define the relative total pressure loss coefficient. The coefficient is given by

$$p_{coefficient} = \frac{p_{r1} - p_{r2}}{p_{r1} - p_{rt1}} \tag{8}$$

where, p_{r1} and p_{rt1} is inlet relative total pressure and relative static pressure respectively, p_{r2} is rotor outlet relative pressure.

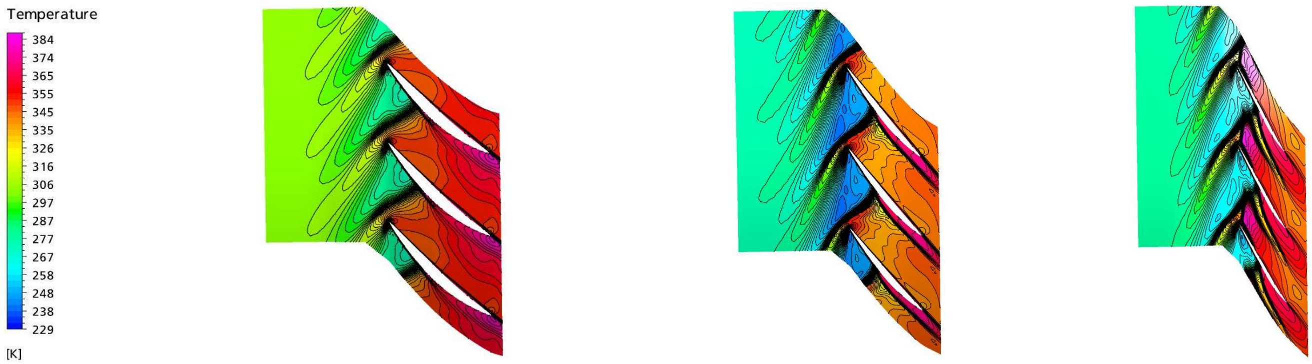

(a) Dry case (Span: left 5%; mid 50%; right 97%)

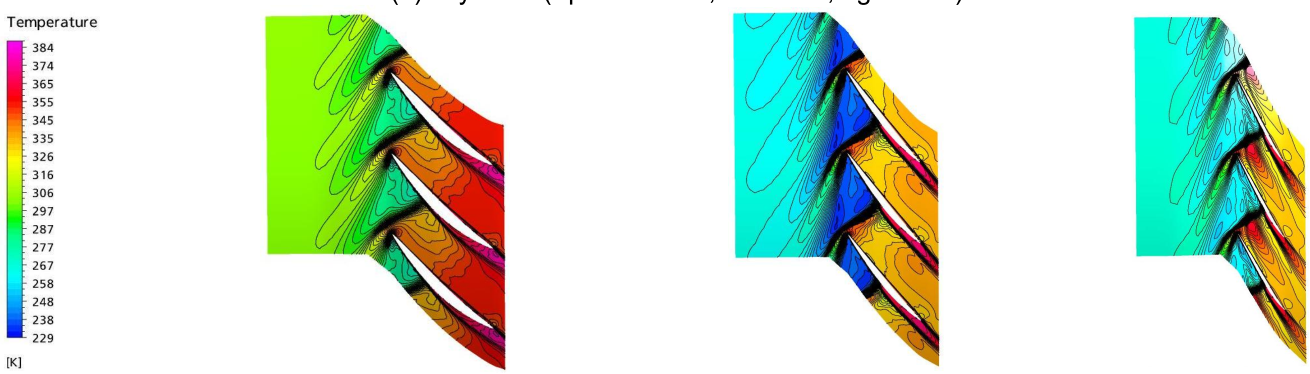

(b) Wet case (Span: left 5%; mid 50%; right 97%)
(Inlet injection: R-R size 5μm; 0.5% of the inlet total mass flowrate)

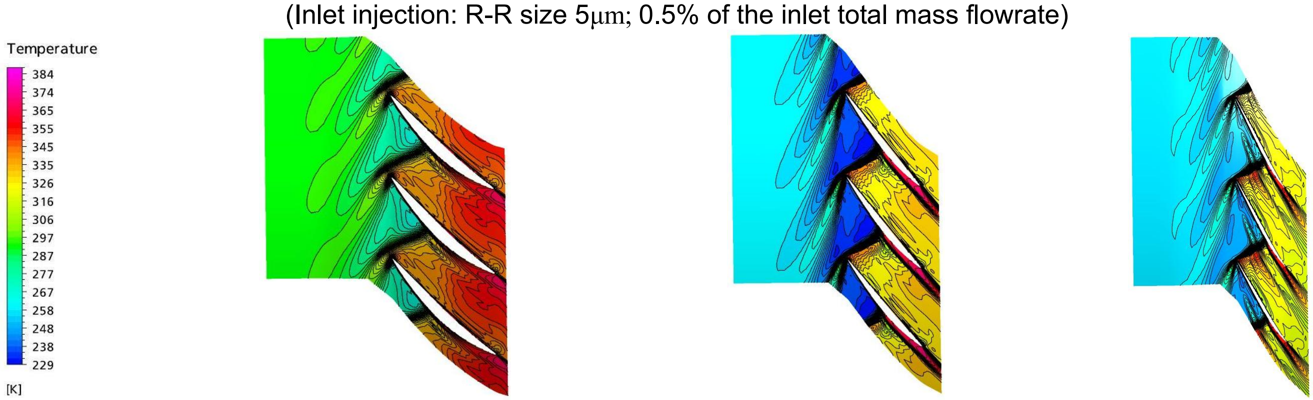

(c) Wet case (Span: left 5%; mid 50%; right 97%)
(Inlet injection: R-R size 5μm; 2% of the inlet total mass flowrate)

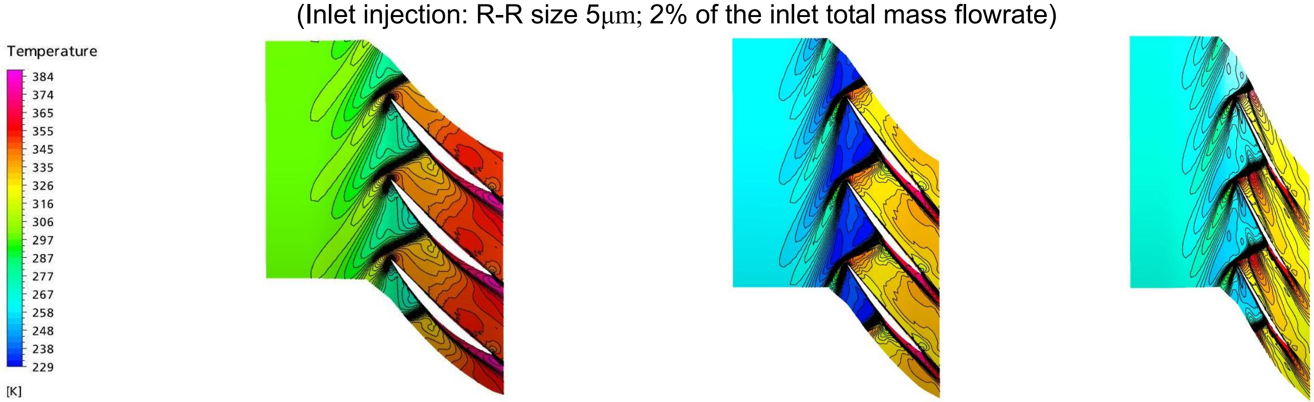

(d) Wet case (Span: left 5%; mid 50%; right 97%)
(Inlet injection: R-R size 8μm; 2% of the inlet total mass flowrate)

Fig. 10 Contours of Temperature on the rotor blade to blade surfaces – All dry cases at the stall boundary

S3 surface is vertical to the axial direction of the compressor. Figure 11 presents the total pressure loss contours at the rotor blade outlet. From Fig. 11(a), it can be seen that the total pressure loss largely occurring at the boundary layers, especially in the separation region near the rotor blade tip and in the hub area. As shown in Fig. 11(b) to Fig. 11(f), it can be seen that the inlet fogging can reduce the large total pressure loss region and expand the range of blue region where the total pressure loss is smaller than in the other regions. It also can be seen in this paper that 3 micron droplet size (with 2% of the inlet mass flow) is better than the other wet cases in reducing the large total pressure loss region and expanding the range of blue region. So it can be inferred that increasing the inlet fogging flowrate or decreasing the droplet size can reduce the large total pressure losses region and expand the range of blue region (low total pressure losses).

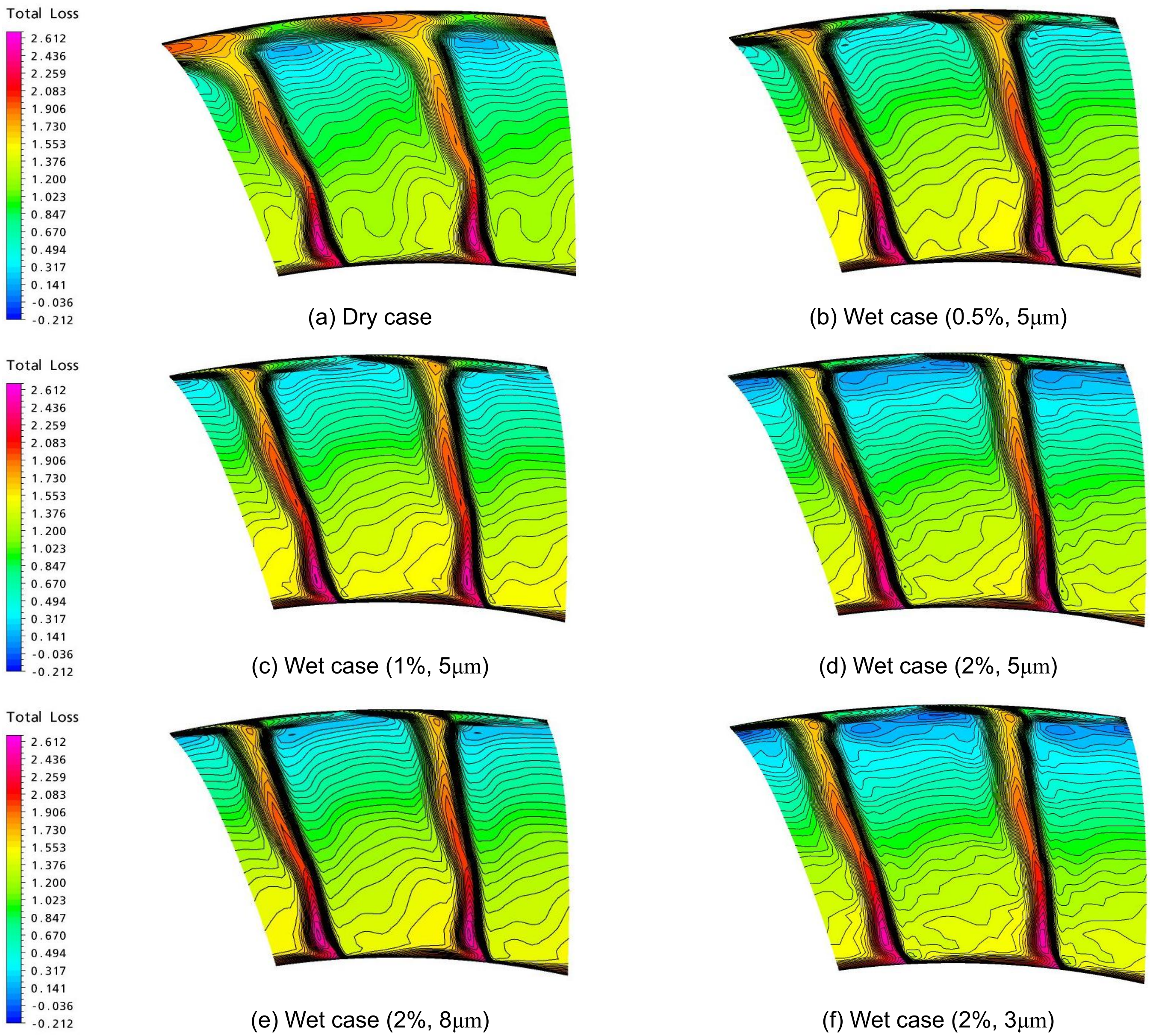

Fig. 11 Contours of the total pressure loss coefficient on S3 surface of rotor outlet – All dry cases at the stall boundary

The tip clearance leakage vortex is an important factor that causes the stall of this transonic compressor stage. Figure 12 shows contours of velocity vector. In Fig. 12(a), there is a circumfluence region at top of this surface and this circumfluence region is the position of the clearance leakage vortex. The circumfluence region could be abated even eliminated by inlet fogging (from Fig. 12(b) to Fig, 12(d)), it also can be seen that the tendency of eliminating the circumfluence region increases with decreasing of the droplet size or increasing of the fogging flowrate. Figure 13 shows the comparison of rotor blade loads distribution for the dry and wet cases under different fogging flowrates and droplet sizes. Inlet fogging makes the shock wave position moving downstream on the suction surface and the tendency of moving shock wave is increased by increasing of the fogging flowrate and decreasing of the droplet size. From above, it can be seen that the shock wave position could affect the inlet flowrate. Form the results discussed in Fig. 13, we know that inlet fogging makes the shock wave position move back, it means that at the stall boundary, inlet fogging improves the inlet flowrate under the same pressure. The static pressure distribution further shows redistribution of the blade loading in the first 50% of the blade chord length and the observed trend is similar for increased fogging flowrate and the droplets sizes. From Fig. 12, the downstream moving of the shock wave position gives leakage flows more acceleration time, then increases the inlet flowrate so that the clearance leakage vortex could be abated or eliminated.

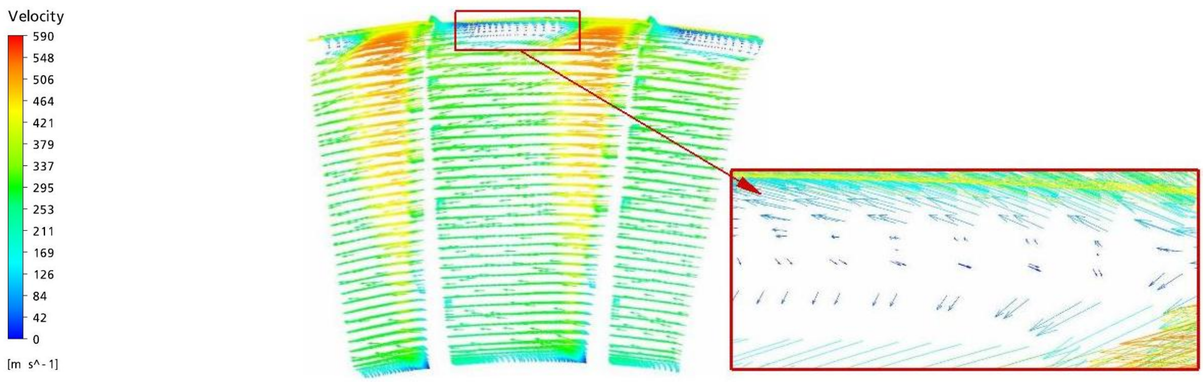

(a) Dry case

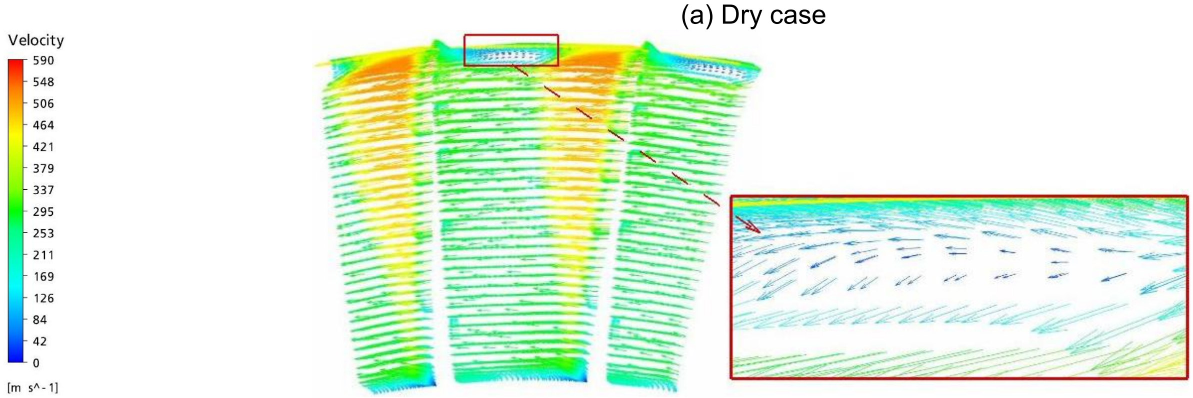

(b) Wet case (0.5%, 10μm)

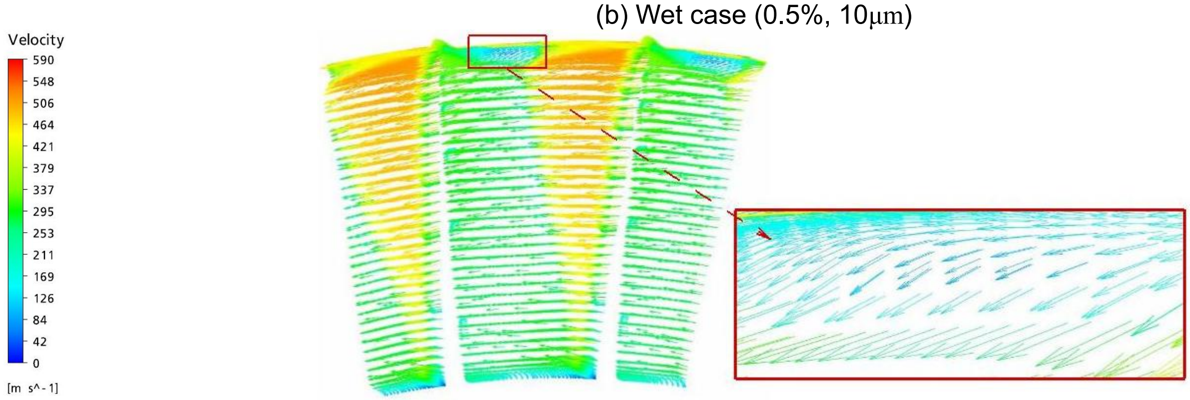

(c) Wet case (1%, 10μm)

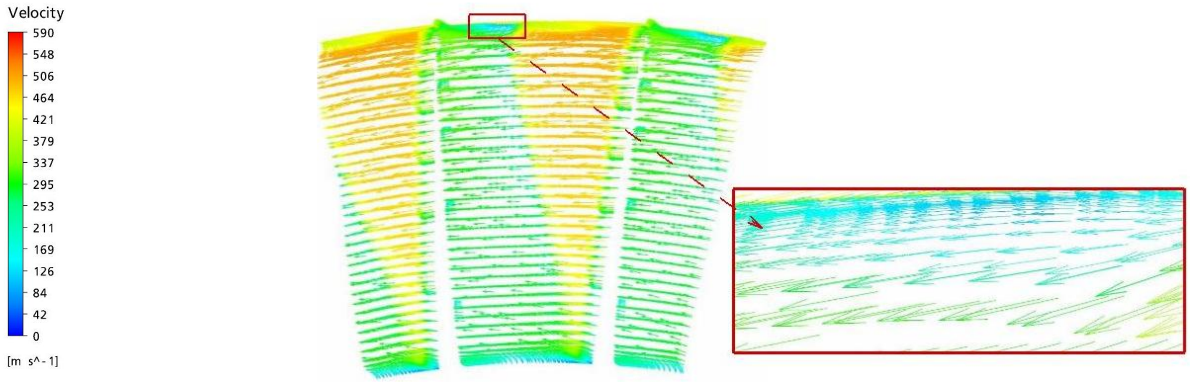

(d) Wet case (1%, 5μm)

Fig. 12 Contours of velocity vector on S3 surface of clearance leakage vortex position – All dry cases at the stall boundary

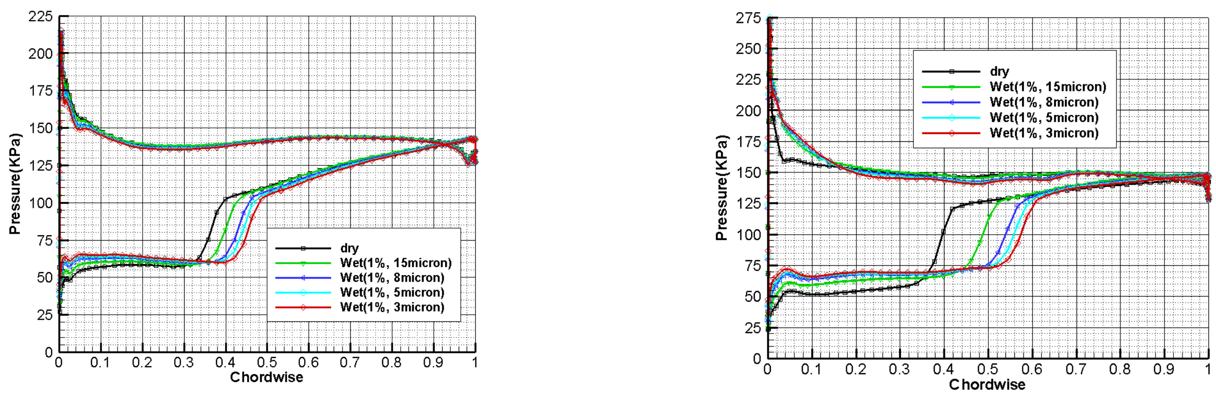

(a) Wet case (Span: left 50%; right 97%)(Inlet injection: 1% of the inlet total mass flowrate)

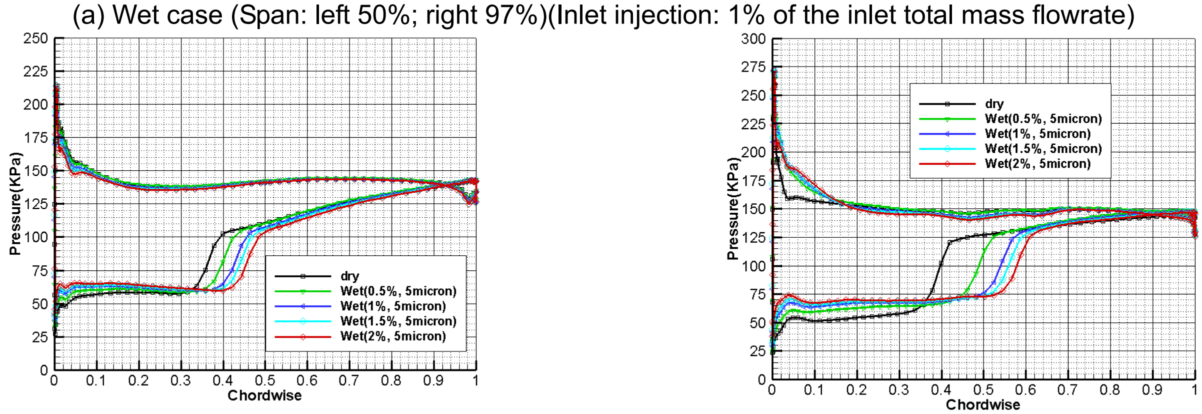

(b) Wet case (Span: left 50%; right 97%)(Inlet injection: R-R size 5μm)

Fig. 13 Rotor blade loads under different fogging conditions

2. Stage performance with inlet fogging at the choking boundary of dry compression

Figure 14 shows the inlet total mass flowrate of dry (20.673kg/s) and wet cases. The numerical simulation shows that the inlet fogging could decrease the inlet mass flowrate under choking conditions. However, the droplet diameter has a little effect on the inlet mass flowrate as shown in Fig. 14(a). But as for the change of fogging flowrate from 0.5% to 2% of the inlet mass flowrate, the mass flowrate of dry choking boundary will decrease.

Figure 15 shows that the inlet fogging at the choking boundary can reduce the stage adiabatic efficiency. The results show that the stage adiabatic efficiency is lower than the dry case at the choking boundary under different fogging conditions except when the inlet fogging flow rate is high (2% or higher) and the droplets size is 3 microns (see Fig. 15). It can also be seen in Fig. 15 that efficiency is improved by increasing the fogging flowrate and by decreasing the droplet size.

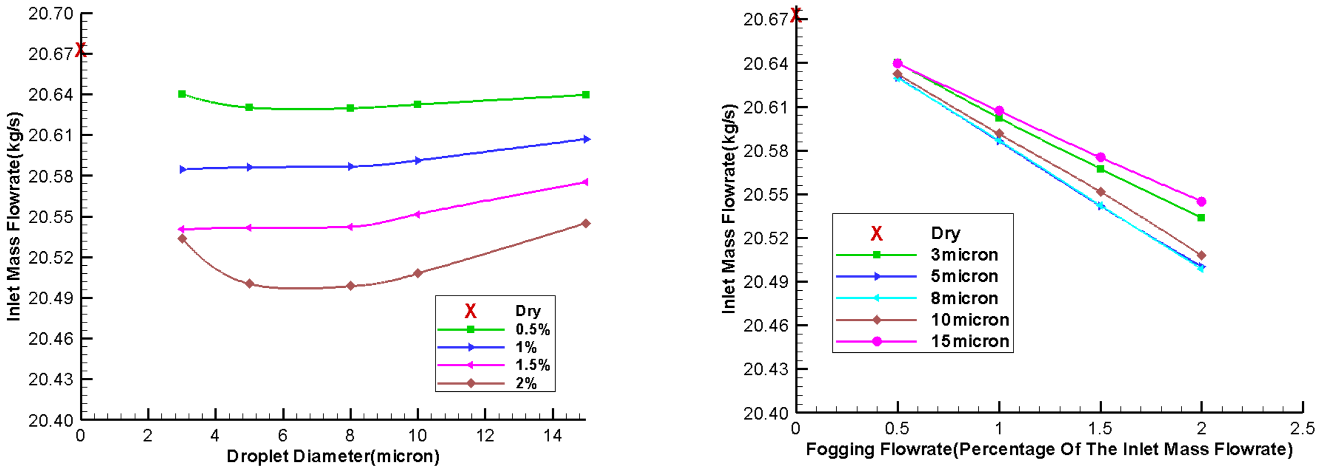

(a) (b)

Fig. 14 Comparison of inlet mass flowrate under different inlet fogging conditions at the choking boundary

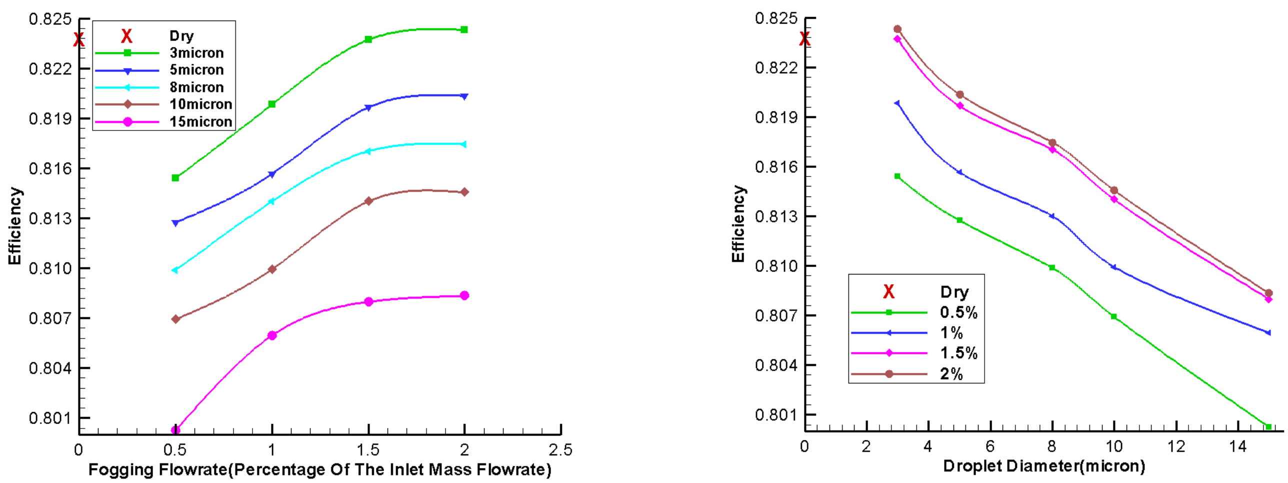

(a) (b)

Fig. 15 Comparison of the stage adiabatic efficiency under different inlet fogging conditions – All dry cases at the choking boundary

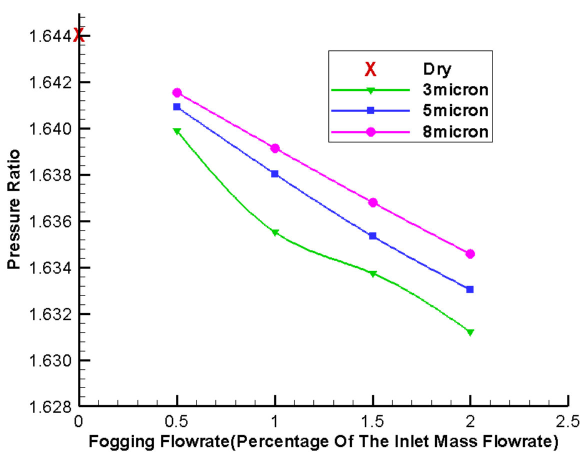

Fig. 16 Comparison of the stage total pressure ratio under different inlet fogging conditions – All dry cases at the choking boundary

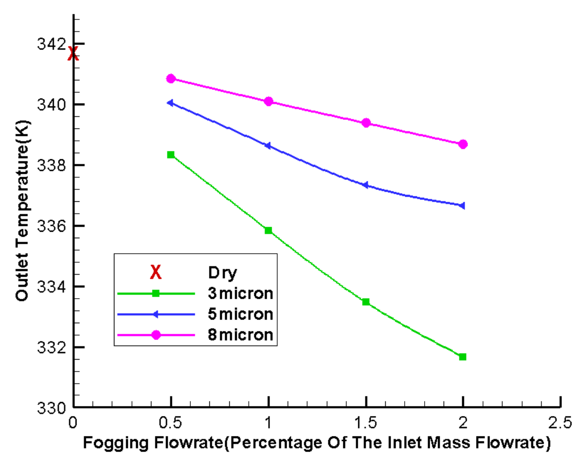

Fig. 17 Comparison of the stage outlet temperature under different inlet fogging conditions – All dry cases at the choking boundary

Compared to the dry case (for which the stage total pressure ratio is 1.644) at the choking boundary, Fig. 16 shows a decreasing trend in the total pressure ratio for all the wet cases irrespective of the droplets size and the fogging flow rate.

Fig. 17 shows that inlet fogging can reduce outlet temperature with increasing of the inlet fogging flowrate and decreasing of the droplet size. Compared to dry case (341.665K), the stage outlet temperature can be reduced to 331.55K when the droplet size is 3 micron and the fogging flowrate is 2% of the inlet mass flowrate. It also can be seen that as the fogging flowrate increases, the outlet temperature continuously reduces.

Fig. 18 and Fig. 19 present the contours of static pressure and temperature for dry and wet cases, respectively on the blade-to-blades surfaces of the rotor and stator. For all the wet cases, the starting dry case is considered at the choking boundary.

Inlet flowrate reaches maximum at the choking boundary. A very large negative incidence forms as air enters into the stator. The large negative incidence makes whole blade passage into an equivalent resizing passage which causes static pressure reducing in the stator blade passage. So the stator blade passage can't play the role of pressure increasing. In Fig. 18, it can be seen that on the surface of span 5%, 50%, 97% the value of static pressure at stator exit is less than value of the stator inlet and inlet fogging can't weaken or eliminate this phenomenon. To the contrary, the pressure reducing tendency at the stator blade exit increases with increase in the fogging flowrate. In Fig. 18(a), shock wave appears at the posterior segment of stator blade passage and this appearance is particularly evident on the surface of span 50%. In Fig. 18(b), (c) and (d), inlet fogging can't make this state changes.

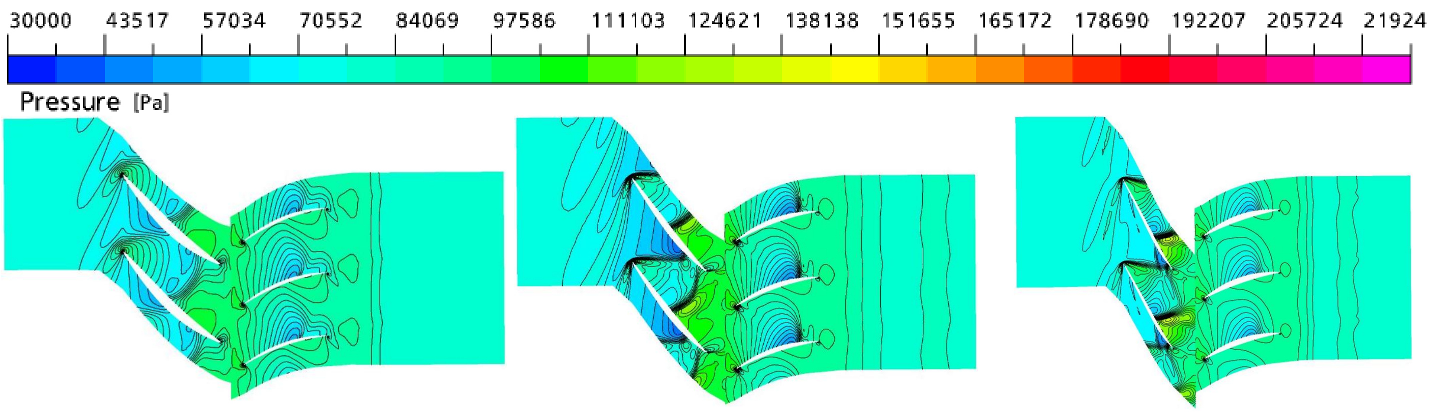

(a) Dry case (Span: left 5%; mid 50%; right 97%)

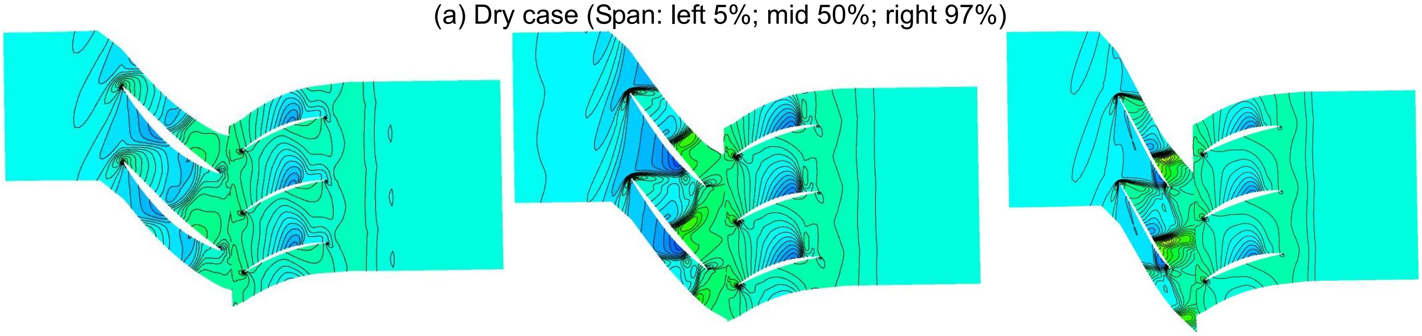

(b) Wet case (Span: left 5%; mid 50%; right 97%)
(Inlet injection: R-R size 3μm; 0.5% of the inlet total mass flowrate)

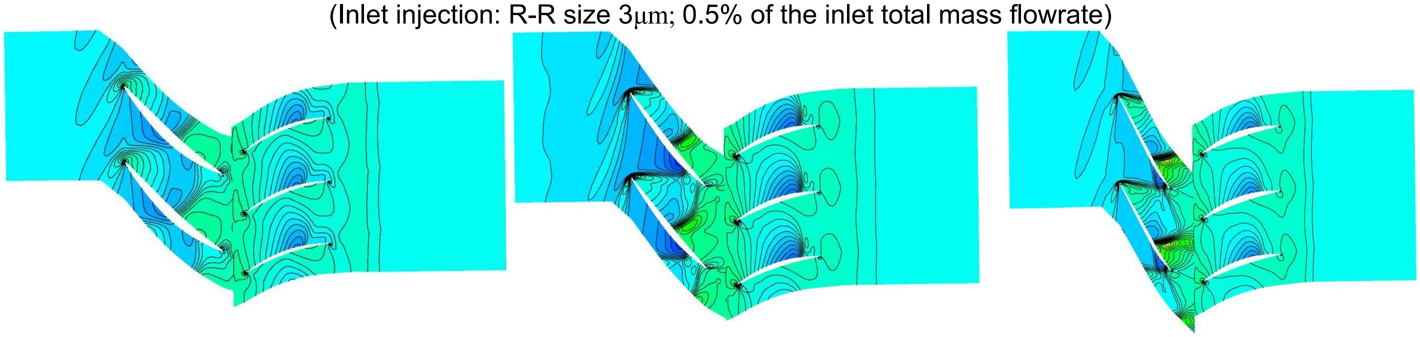

(c) Wet case (Span: left 5%; mid 50%; right 97%)
(Inlet injection: R-R size 3μm; 2% of the inlet total mass flowrate)

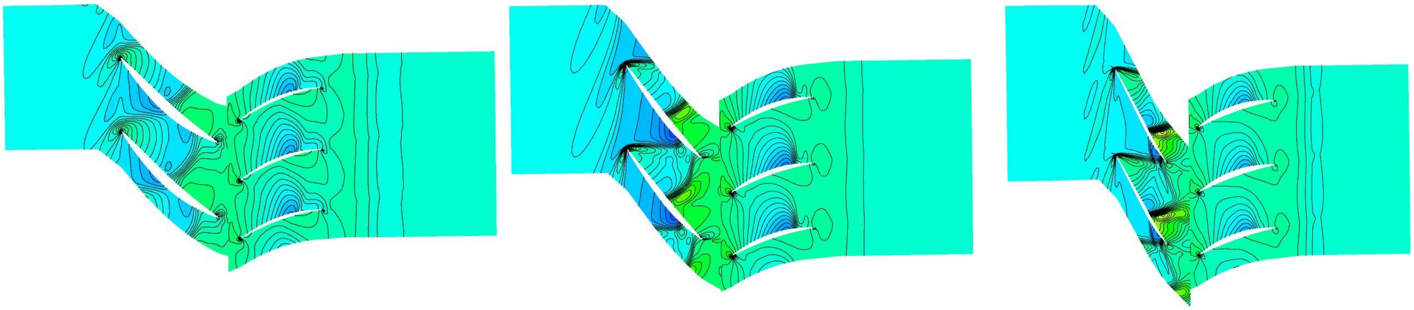

(d) Wet case (Span: left 5%; mid 50%; right 97%)
(Inlet injection: R-R size 5μm; 2% of the inlet total mass flowrate)

Fig. 18 Contours of static pressure on blade to blade surfaces under dry and wet conditions – All dry cases at the choking boundary

From Fig. 19, it can be seen that the temperature behind the shock wave on the rotor blade to blade surfaces of span 5%, 50% and 97% of wet cases are lower than the dry case. On the rotor blade to blade surfaces of 97%, a high temperature region appears behind the shock wave in the dry case and the inlet fogging can reduce this high temperature region and the tendency of reducing the high temperature region can be increased when the fogging flowrate increases or droplet size decreases. As shown in Fig. 19, the increasing of fogging flowrate or decreasing of droplet diameters significantly reduces the temperature in the whole passage of the stator.

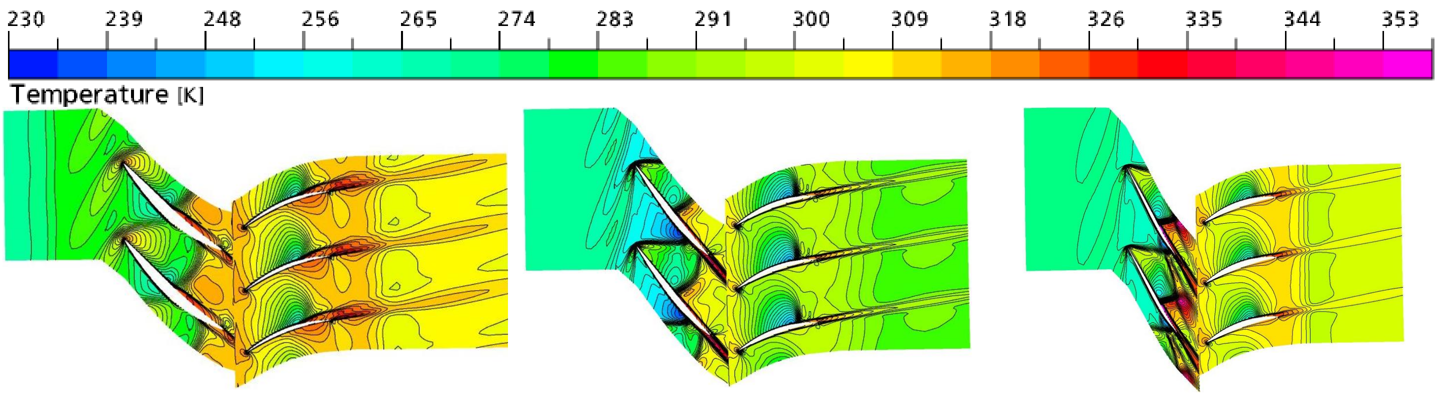

(a) Dry case (Span: left 5%; mid 50%; right 97%)

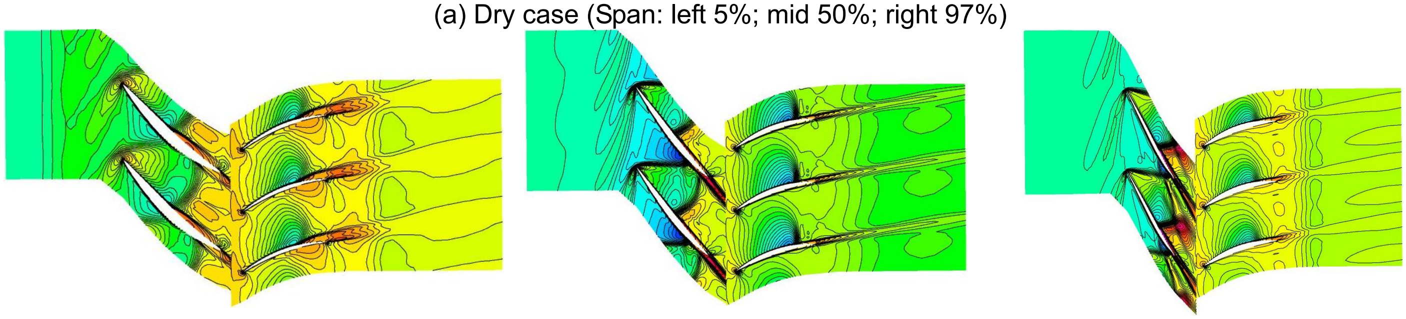

(b) Wet case (Span: left 5%; mid 50%; right 97%)
(Inlet injection: R-R size 3μm; 0.5% of the inlet total mass flowrate)

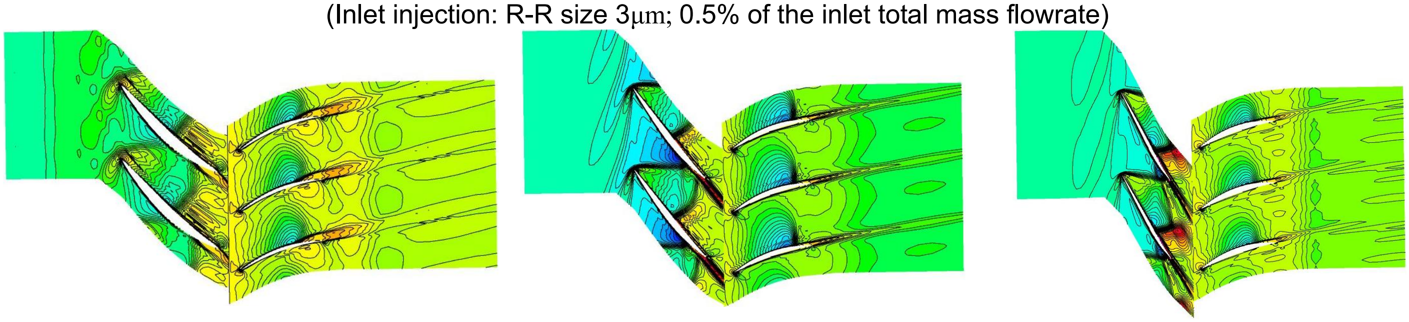

(c) Wet case (Span: left 5%; mid 50%; right 97%)
(Inlet injection: R-R size 3μm; 2% of the inlet total mass flowrate)

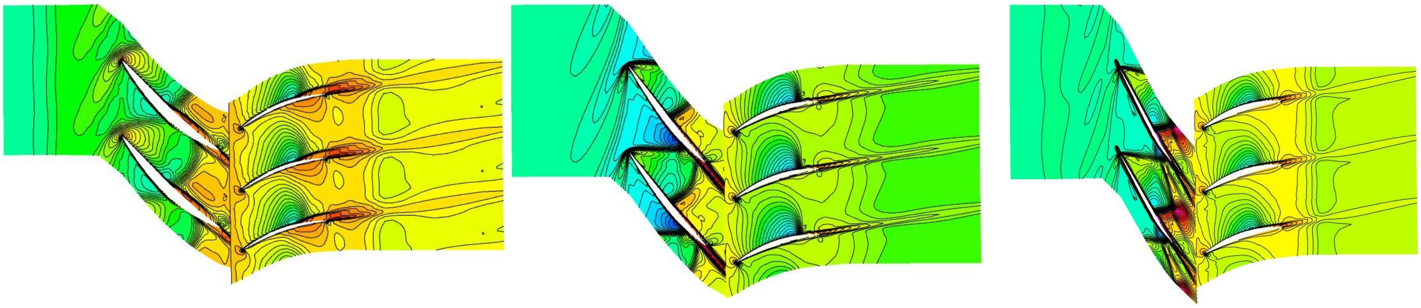

(d) Wet case (Span: left 5%; mid 50%; right 97%)
(Inlet injection: R-R size 5μm; 2% of the inlet total mass flowrate)

Fig. 19 Contours of Temperature on blade to blade surfaces under dry and wet conditions – All dry cases at the choking boundary

Fig. 20 presents the total pressure loss contours at the rotor blade outlet. From Fig. 20(a) to Fig. 20(d), it can be seen that the inlet fogging expands the high total pressure loss region at the blade hub areas with increasing of the fogging flowrate or decreasing of the droplet size. It also can be seen that inlet fogging reduces the blue region (low total pressure loss region) near the blade's tip.

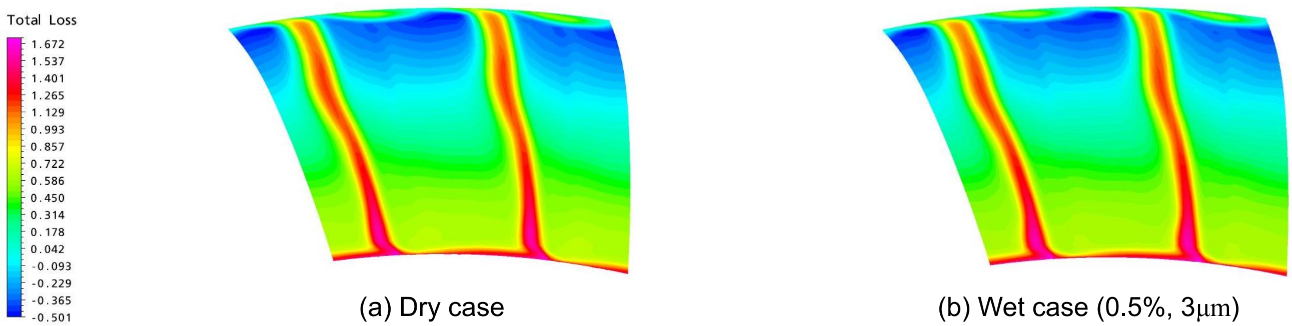

(a) Dry case (b) Wet case (0.5%, 3μm)

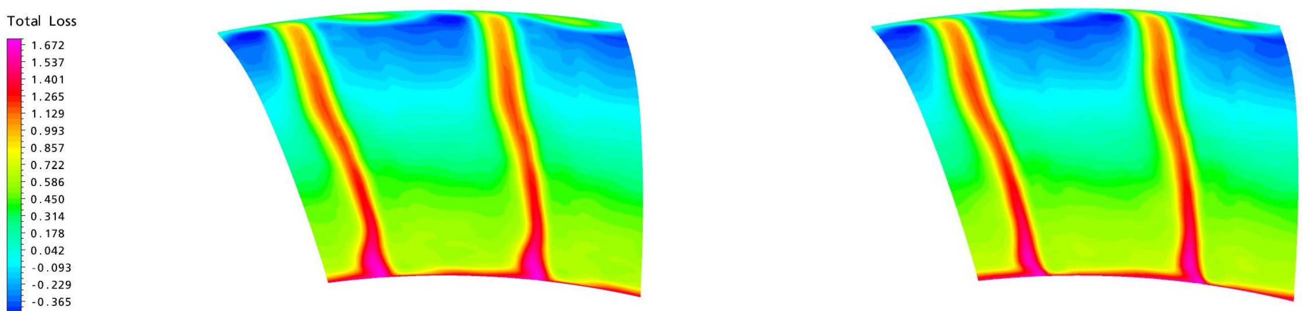

(c) Wet case (2%, 3μm) (d) Wet case (2%, 5μm)

Fig. 20 Contours of the total pressure loss coefficient on blade outlet surface

Fig. 21 is the comparison of limiting streamlines on stator suction surface for the dry case and some wet cases. In Fig. 21(a), near the top, root and the central part of the stator trailing edge, it appears big range of separation. It also can be seen that shock wave appears near the stator trailing edge. From Fig. 21(b) and (c), it can be seen that the fogging droplet of 5 micron diameter decreases the separation near the central part of the tailing edge. Furthermore, it can be seen that the separation near the central portion of the trailing edge decreases or diminishes with increasing of the fogging flowrate. Figure 21(d) shows that the fogging droplet of 10 micron diameter intensifies the separation near the central portion of the tailing edge.

At the choking boundary, a very large negative incidence causes flow separation on the rotor pressure surface. Figure 22 is a comparison of velocity vector patterns on the rotor blade to blade surfaces under different fogging mass flowrates and droplet diameters. In Fig. 22(a), we can see that a separation region appears at the rotor pressure surface. From Fig. 22(a) to Fig. 22(c), it could be seen that as the fogging flowrates increases, the separation region fades away compared to the dry compression especially in Fig. 22(c). When the fogging flowrate is 0.5% of the inlet mass flowrate, the separation region decreases compared to the dry compression and the separation region can not be seen anymore when the fogging flowrate is 2% of the inlet mass flowrate. In Fig. 22(c), Fig. 22(e) and Fig. 22(f), the separation gradually disappears and this separation region narrows as the droplet diameter decreases.

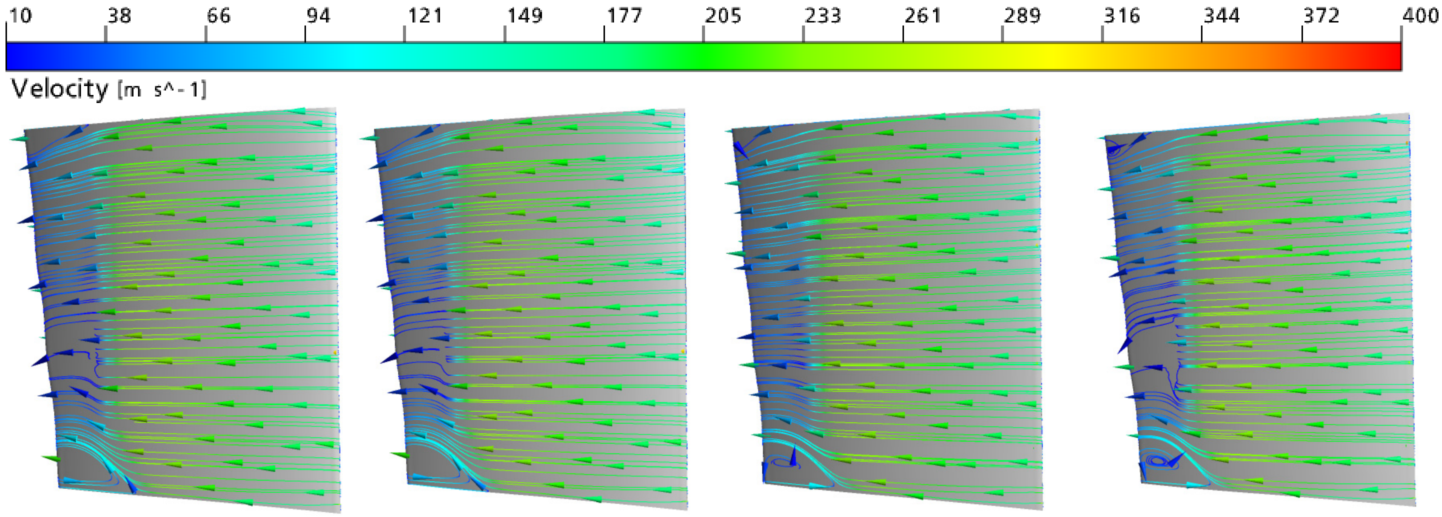

(a) Dry case (b) Wet case (0.5%, 5μm) (c) Wet case (2%, 5μm) (d) Wet case (2%, 10μm)

Fig. 21 Limiting streamlines on suction surfaces of the stator blade

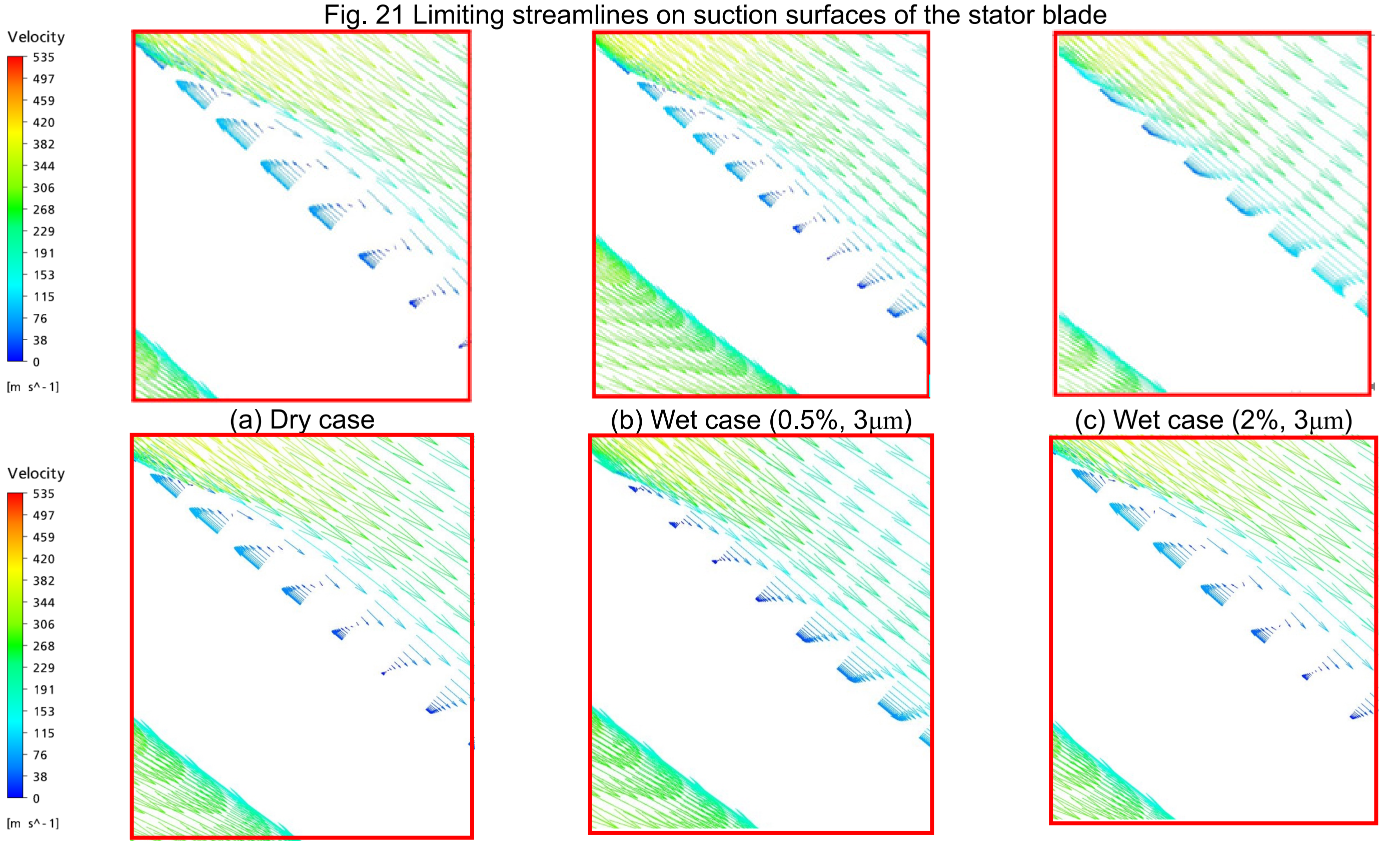

(a) Dry case (b) Wet case (0.5%, 3μm) (c) Wet case (2%, 3μm)

(d) Wet case (0.5%, 5μm) (e) Wet case (2%, 5μm) (f) Wet case (2%, 8μm)

Fig. 22 Partial enlarged contours of velocity vector on rotor blade to blade surface

Figures 23 and 24 present rotor and stator blade loading distribution for dry and wet cases under different droplet sizes and fogging flowrates, respectively. It can be seen that the difference of stator blade loads especially on the surface of span 50% is not evident among dry case and wet cases. In the rotor blade loading figures especially on the surface of span 97%, the pressure value on the suction surface is larger than the value on the pressure surface at the front of shock wave. From the stator blade loading figures (Fig. 23(b) and Fig. 24(b)), it can be seen that near the leading edge the pressure value on pressure surface is lower than the value on suction surface, this is caused by the large negative incidence that make the blade passage into an equivalent resizing passage and inlet fogging can not change this condition. From the rotor blade loading figures (span: 5%, 50%, 97%) and the stator blade loading figures (span: 5%, 97%), inlet fogging makes the shock wave position moving back some distance and the tendency of moving back increases with decreasing of the droplet size and increasing of the fogging flowrate.

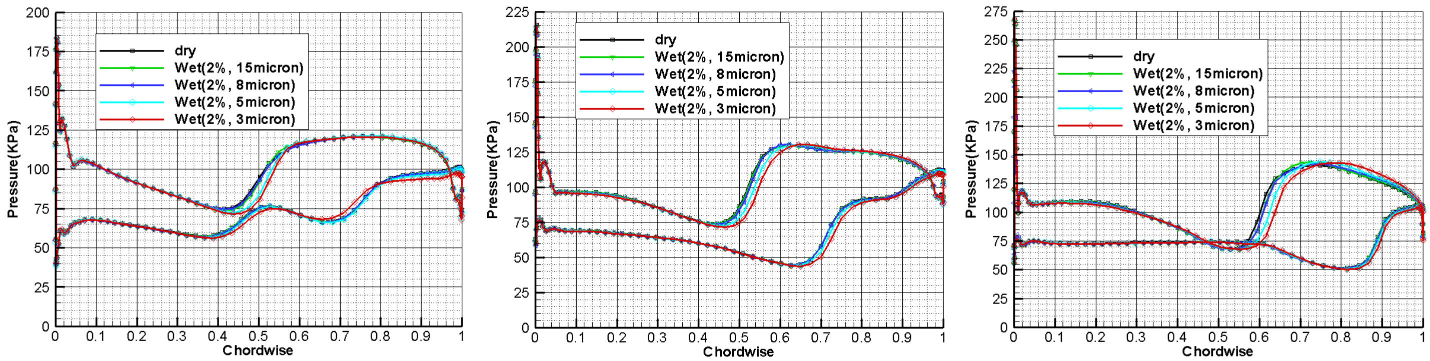

(a) rotor blade loads (Span: left 5%; mid 50%; right 97%)

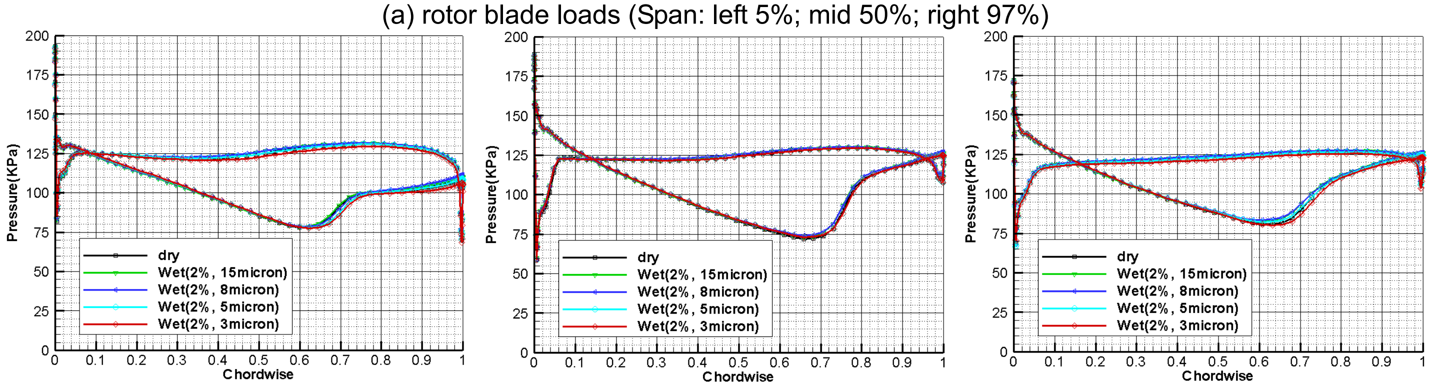

(b) stator blade loads (Span: left 5%; mid 50%; right 97%)

Fig. 23 Blade loads under the water flowrate condition, which is 2% of the inlet total mass flowrate

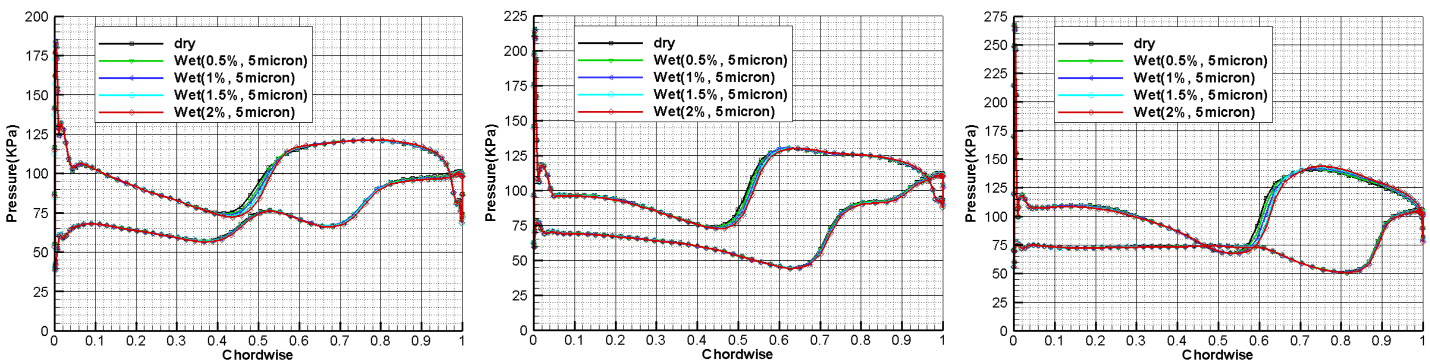

(a) rotor blade loads (Span: left 5%; mid 50%; right 97%)

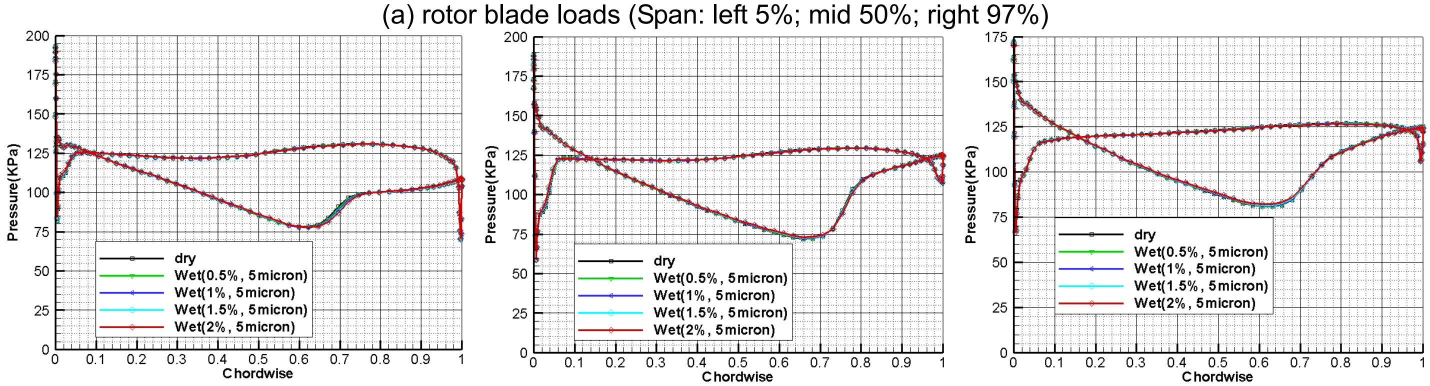

(b) stator blade loads (Span: left 5%; mid 50%; right 97%)

Fig. 24 Blade loads under the water flowrate condition, which droplet diameter is 5micron

CONCLUSIONS

The performances of a transonic compressor stage with inlet fogging at the stall boundary and the choking boundary are studied in this paper using a commercially available CFX program. Effects of important factors such as injected fogging flow rate and droplet size on the stage performance and the 3-D flow fields within a stage passage have been investigated. Based on the investigation, the following main observations can be made:

(1) At the stall boundary, the simulation results shows an augmentation in the total pressure ratio, adiabatic efficiency and a reduction in the outlet temperature for the stage as the fogging flowrate increases or the droplet diameter decreases. Inlet fogging can abate or even eliminate the clearance leakage vortex and makes the shock wave moving downstream compared to the dry case. The results also indicate that the stall boundary of compressor stage could be extended by inlet fogging which contains small size droplets, and the tendency will be expanded by increasing of the inlet fogging flowrate in certain cases.

(2) At the choking boundary, separation appears on the rotor pressure surface and it could be reduced or eliminated by increasing of the fogging flowrate or decreasing of the droplet size. The simulation results shows a reduction in the static pressure, stage total pressure ratio and the outlet temperature as fogging flowrate increases or the droplet size decreases. As the fogging flowrate increases, the decreasing tendency of the outlet temperature continuously reduces. The stage adiabatic efficiency can not be improved by adjusting the fogging flowrate and droplet size under the choking condition. Inlet fogging can not restrain chocking and the results also indicate that inlet fogging will decrease the mass flow at the choking boundary instead of expanding or increasing it.

ACKNOWLEDGEMENT

The authors would like to acknowledge the support of National Natural Science Foundation of China, Grant No. 50776021 and China Doctoral Grant No. 20092304110004. The authors would also like to thank reviewers for their comments which help us improve the quality of this paper. The opinions given in this paper are of the authors and not of their respective organizations.

APPENDIX

GOVERNING EQUATIONS OF CONTINUOUS PHASE

1. The mass conservation equation of the continuous phase

$$\frac{\partial \rho}{\partial t} + \nabla \cdot (\rho \vec{u}) = S_{\mathrm{m}} \tag{A1}$$

where, ρ is the density of continuous phase and $\vec{u}$ is the velocity. The source term S_{m} represents the mass transfer from dispersed second phase to continuous phase due to the vaporization of liquid droplets.

2. Momentum conservation equation of the continuous phase

$$\frac{\partial}{\partial t}(\rho \vec{u}) + \nabla \cdot (\rho \vec{u}\vec{u}) = -\nabla p + \nabla \cdot (\bar{\bar{\tau}}) + \vec{F} \tag{A2}$$

where, p is static pressure and $\vec{F}$ is external body forces (Here, e.g., the interaction with the water droplets means the momentum transfer from the water droplets to the continuous phase).

$\bar{\bar{\tau}}$ is the viscous shear stress tensor given by

$$\bar{\bar{\tau}} = \mu[(\nabla \vec{u} + \nabla \vec{u}^{T}) - \frac{2}{3}\nabla \cdot \vec{u} I] \tag{A3}$$

where, μ is the dynamic viscosity and I is the unit tensor.

3. Energy conservation equation of the continuous phase

$$\frac{\partial}{\partial t}(\rho h_{\mathrm{t}}) + \nabla \cdot (\vec{u}(\rho h_{\mathrm{t}} + p)) = \nabla \cdot (\lambda \nabla T + (\bar{\bar{\tau}} \cdot \vec{u})) + \vec{u} \cdot \vec{F} + S_{\mathrm{h}} \tag{A4}$$

where, h_{t} is total enthalpy, λ is thermal conductivity and S_h is the heat source. Total enthalpy h_{t} is related to static enthalpy h, by

$$h_{\mathrm{t}} = h + \frac{u^2}{2} \tag{A5}$$

In this paper, specific heats of air and water vapor are defined as polynomial functions of temperature.

GOVERNING EQUATIONS OF DISPERSED PHASE

1. Motion equation of droplets

For the study in this article, the motion equation of droplet that is written in a rotating Lagrangian reference frame can be written as:

$$m_{\mathrm{p}} \frac{\mathrm{d}\vec{u}_{\mathrm{p}}}{\mathrm{d}t} = \vec{F}_{\mathrm{D}} + \vec{F}_{\mathrm{R}} \tag{A6}$$

where, m_{p} is mass of droplet, $\vec{u}_{\mathrm{p}}$ is velocity of droplet, $\vec{F}_{\mathrm{D}}$ is drag force acting on the particle and $\vec{F}_{\mathrm{R}}$ are forces due to domain rotation (centrifugal and Coriolis forces). $\vec{F}_{\mathrm{R}}$ and $\vec{F}_{\mathrm{D}}$ are written as:

$$\vec{F}_{\mathrm{R}} = m_{\mathrm{p}}\left[-\vec{\omega} \times (\vec{\omega} \times \vec{r}) - 2\vec{\omega} \times \vec{u}_{\mathrm{p}}\right] \tag{A7}$$

$$\vec{F}_{\mathrm{D}} = C_{\mathrm{D}}(\vec{u} - \vec{u}_{\mathrm{p}}) \tag{A8}$$

where, $\vec{\omega}$ is the rotating speed, $\vec{r}$ is the position vector and C_{D} is drag coefficient. The relative Reynolds number of droplet is defined as:

$$Re_{\mathrm{p}} = \frac{\rho d_{\mathrm{p}} \left|\vec{u}_{\mathrm{p}} - \vec{u}\right|}{\mu} \tag{A9}$$

where, d_{p} is the droplet diameter. Then the value of C_{D} can be determined by the following law:

In the viscous region, Re_{p}<0.1,

$$C_D = 24/Re_p\,, \tag{A10}$$

In the transitional region, $0.1<Re_p<1\,000$,

$$C_D = \max\left(24/Re_p(1+0.15Re_p^{0.687}),0.44\right), \tag{A11}$$

In the inertial region, $1\,000 \le Re_p$,

$$C_D = 0.44\,, \tag{A12}$$

2. Heat transfer equation of the dispersed phase

The rate of temperature change for the particle can be obtained from the following equation:

$$m_p C_w \frac{dT_p}{dt} = \pi d_p \lambda Nu(T - T_p) + \frac{dm_p}{dt} h_{fg} \tag{A13}$$

where, C_w is the specific heat of water, T_p is the temperature of droplet, λ is the thermal conductivity of the continuous phase, Nu is the Nusselt number, dm_p/dt is the rate of change of mass transfer and h_{fg} is the latent heat of vaporization. And Nu is given by

$$Nu = 2 + 0.6Re^{0.5}(\mu \frac{C_p}{\lambda})^{1/3} \tag{A14}$$

The two terms of right hand of Eq. (16) are convective heat transfer and latent heat transfer associated with mass transfer respectively.

3. Mass transfer equation of the dispersed phase

The evaporation model uses two mass transfer correlations depending on whether the droplet is above or below the boiling point. This is determined through the Antoine equation given below:

$$\log_{10} p_{sat} = A - \frac{B}{T + C - 273.15} \tag{A15}$$

where, *A,B and C* are constant coefficients [29].

When the particle is above the boiling point, the rate of mass transfer is determined by the convective heat transfer:

$$\frac{dm_p}{dt} = -\frac{\pi d_p \lambda Nu(T - T_p)}{h_{fg}} \tag{A16}$$

When the particle is below the boiling point, the rate of mass transfer is given by the formula below:

$$\frac{dm_p}{dt} = \pi d_p \rho_v D_v Sh \frac{M_v}{M} \log(\frac{1-f_p}{1-f}) \tag{A17}$$

where, ρ_v , D_v are density and diffusivity of vapor, Sh is the Sherwood number, M_v and M are respectively the molecular weights of the vapor and the mixture in the continuous phase, and f_p and f are the molar fractions in the droplet and in the gas phase. And Sh is given by:

$$Sh = 2 + 0.6Re^{0.5}(\frac{\mu}{\rho_v D_v})^{1/3} \tag{A18}$$

NOMENCLATURE

C_D	drag coefficient [-]
C_p	specific heat of constant pressure [$J/(kg\cdot K)$], 1006.43 and 2014 for gas and water vapor respectively, here
C_w	specific heat of water droplet [$J/(kg\cdot K)$]
d_p	droplet diameter [m]
f	steam-to-air (or water-to-air) ratio (-)
$\vec{F}$	external body force [$kg/(m^2\cdot s^2)$]
$\vec{F}_D$	drag force [$kg/(m^2\cdot s^2)$]
$\vec{F}_R$	domain rotation forces [$kg/(m^2\cdot s^2)$]
f_p	molar fraction in the droplet [-]
f	molar fraction in the gas phase [-]
h	static enthalpy [J/kg]
h_t	total enthalpy [J/kg]
h_{fg}	specific latent heat of evaporation [J/kg]
I	unit tensor [-]
M_t	torque on the rotor ($N\cdot m$), which is given by the program directly
M_V	molecular weights of the vapor [kg/mol]
M	molecular weights of the mixture [kg/mol]
m_{in}	stage inlet mass flowrate (kg/s)
m_p	mass of droplet [kg]
Nu	Nusselt number
p	static pressure (Pa)
p_{r1}	inlet relative total pressure (Pa)
p_{r2}	rotor outlet relative total pressure (Pa)
p_{rt1}	inlet relative static pressure (Pa)
p_{sat}	saturation pressure of vapor [Pa]
R	universal gas constant [8.31447 $J/(mol\cdot K)$]
$\vec{r}$	position vector in the rotating frame [m]
r	the radius of droplet [m]
S^0	static entropy [$J/(kg\cdot k)$]
S_h	source term of energy [$J/(m^3\cdot s)$]
S_m	source term of mass [$kg/(m^3\cdot s)$]
T_p	temperature of droplet [K]
$\vec{u}$	continuous phase velocity [m/s]
$\vec{u}_p$	droplet velocity [m/s]
W_a	specific compression work of gas component (J/kg)
W_v	specific compression work of vapor component (J/kg)
W_{wi}	Isentropic specific work of wet compression (J/kg)
W_w	actual specific work of wet compression (J/kg)
$\overline{\overline{\tau}}$	stress tensor [Pa]
Re_p	the relative Reynolds number of droplet [-]
Sh	Sherwood number[-]

λ	heat conductivity [$W/(m \cdot K)$]
μ	dynamic viscosity of the continuous phase [$Pa \cdot S$]
ρ	density of continuous phase [kg/m^3]
ρ_g	density of gas [kg/m^3]
ρ_p	density of the droplet [kg/m^3]
σ	surface tension [N/m]
ω	rotational speed [rad/s]
γ	ratio of specific heat, 1.4 and 1.33 for air and water vapor respectively

REFERENCES

[1] Bagnoli, M., Bianchi, M., Melino, F., Peretto, A., Spina, P. R., Bhargava, R., and Ingistov, S., 2004, "A Parametric Study of Interstage Injection on GE Frame 7EA Gas Turbine", ASME Paper No. GT2004-53042

[2] Hartel, C. and Pfeiffer, P., 2003, "Model Analysis of High-Fogging Effects on the Work of Compression", ASME Paper No. GT2003-38117

[3] White, A. J. and Meacock, A. J., 2003, "An Evaluation of the Effects of Water Injection on Compressor Performance", ASME Paper No. GT2003-38237

[4] Horlock, J. H., 2001, "Compressor Performance with Water Injection", ASME Paper No. 2001-GT-0343

[5] Roumeliotis, I. and Mathioudakis, K., 2005, "Evaluation of Interstage Water Injection Effect of Compressor and Engine Performance", ASME Paper No. GT2005-68698

[6] Tawney, R., Pearson, C., and Brown, M., 2001, "Options to Maximize Power Output for Merchant Plants in Combined Cycle Applications", ASME Paper No. 2001-GT-0409

[7] Bhargava, R. K., Meher-Homji, C. B., Chaker, M. A., Bianchi, M., Melino, F., Peretto, A., and Ingistov, S., 2005, "Gas Turbine Fogging Technology - A State-of-the-Art Review, Part I: Inlet Evaporative Fogging–Analytical and Experimental Aspects", ASME Paper No. GT2005-68336

[8] Brun, K., Gonzalez, L. E., and Platt, J. P., 2008, "Impact of Continuous Inlet Fogging and Overspray Operation on GE 5002 Gas Turbine Life and Performance", ASME Paper No. GT2008-50207

[9] Chaker, M. and Meher-Homji, C. B., 2008 "Gas Turbine Power Augmentation-Parametric Study Relating to Fog Droplet Size and Its Influence on Evaporative Efficiency", ASME Paper No. GT2008-51476

[10] Bhargava, R. K., Bianchi, M., Melino, F., Peretto, A., and Spina, P. R., 2008, "Influence of Compressor Performance Maps Shape on Wet Compression", ASME Paper No. GT2008-50761

[11] Meher-Homji, C. B. and Mee III, T. R., 2000, "Inlet Fogging of Gas Turbine Engines, Part A: Theory, Psychrometrics, and Fog Generation", ASME Paper No. 2000-GT-307

[12] Meher-Homji, C. B. and Mee III, T. R., 2000, "Inlet Fogging of Gas Turbine Engines, Part B: Practical Considerations, Control, and O&M Aspects", ASME Paper No. 2000-GT-308

[13] Fabbrizzi, M., Cerretelli, C., Medico, F. D., and D'Orazio, M., 2009, "An Experimental Investigation of a Single Stage Wet Gas Centrifugal Compressor", ASME Paper No. GT2009-59548

[14] Shibata, T., Takahashi, Y., and Hatamiya, S., 2008, "Inlet Air Cooling with Overspray Applied to a Two-stage Centrifugal Compressor", ASME Paper No. GT2008-50893

[15] Roumeliotis, R. and Mathioudakis, F., 2006, "Water Injection Effects on Compressor Stage Operation", ASME Paper No. GT2006-90427

[16] Bhargava, R. K., Meher-Homji, C. B., Chaker, M. A., Bianchi, M., Melino, F. and Peretto, A., and Ingistov, S., 2005, "Gas Turbine Fogging Technology-A State of the Art Review, Part II: Overspray Fogging-Analytical and Experimental Aspects", ASME Paper No. GT2005-68337

[17] Chaker, M., Meher-Homji, C. B., and Mee III, T. R., 2003, "Inlet Fogging of Gas Turbine Engines-Experimental and Analytical Investigations on Impaction Pin Fog Nozzle Behavior", ASME Paper No. GT2003-38801

[18] Ulrichs, E. and Joos, F., 2006, "Experimental Investigations of the Influence of Water Droplets in Compressor Cascades", ASME Paper No. GT2006-90411

[19] Eisfeld, T. and Joos, F., 2009, "Experimental Investigation of Two-Phase Flow Phenomena in Transonic Compressor Cascades", ASME Paper No. GT2009-59365

[20] Zheng, Q., Sun, Y., Li, S., and Wang, Y., 2002, "Thermodynamic Analysis of Wet Compression Process in the Compressor of Gas Turbine", ASME Paper No. GT-2002-30590

[21] Sun, L., Li, Y., Zheng, Q., and Bhargava, R., 2008, "The Effects of Wet Compression on the Separated Flow in a Compressor Stage", ASME Paper No. GT2008-50920

[22] Shao, Y., Zheng, Q., and Zhang, Y., 2006, "Numerical Simulation of Aerodynamic Performances of Wet Compression Compressor Cascade", ASME Paper No. GT2006-91125

[23] Bhargava, R. and Meher-Homji, C. B., 2002, "Parametric Analysis of Existing Gas Turbines with Inlet Evaporative and Overspray Fogging", ASME Paper No. GT-2002-30560

[24] Sexton, W. R. and Sexton, M. R., 2003, "The Effects of Wet Compression on Gas Turbine Engine Operating Performance", ASME Paper No. GT2003-38045

[25] Zheng, Q., Li, M., and Sun, Y., 2003, "Thermodynamic Performance of Wet Compression and Regenerative (WCR) Gas Turbine", ASME Paper No. GT2003-38517

[26] Reid, L. and Moore, R. D., 1978, "Design and Overall Performance of Four Highly-Loaded, High-Speed Inlet Stages for an Advanced, High-Pressure-Ratio Core Compressor", NASA TP-1337

[27] Reid, L. and Moore, R. D., 1978, "Performance of Single-

Stage Axial-Flow Transonic Compressor With Rotor and Stator Aspect Ratios of 1.19 and 1.26, Respectively, and With Design Pressure Ratio of 1.82", NASA TP-1338
[28] Moore, R. D. and Reid, L., 1980, "Performance of Single-Stage Axial-flow Transonic Compressor with Rotor and Stator Aspect Ratios of 1.19 and 1.26, Respectively, and with Design Pressure Ratio of 2.05", NASA TP-1659
[29] Moran, M. J. and Shapiro, H. N., 2006, Fundamentals of Engineering Thermodynamics, 5th Edition, John Wiley & Sons Inc., Chichester; pp. 755
[30] B.E. Launder and D.B. Spalding. Lectures in Mathematical Models of Turbulence [M]. Academic Press, London, England, 1972.

